MASTER THESIS

Development of a cell formation system

Author:
Tobias Kull

Submitted at:
Institute of Electrical Engineering (ETI)
Karlsruhe Institute of Technology
“Energietechnik“
Instituto Technológico de Buenos Aires
“Maestría en Energía y Ambiente“

Supervisors:
Prof. Dr.-Ing. Marc Hiller, M.Sc. Manuel Baena

Karlsruhe, 06.11.2017

Declaration of authorship

I declare that this thesis has been composed solely by myself and under consideration of the rules for protection of good scientific practice of the Karlsruhe Institute of Technology (KIT). It has not been submitted, in whole or in part, in any previous application for a degree. Unless stated otherwise by reference or acknowledgment, the work presented is entirely my own**.**

Ich versichere hiermit, dass ich meine Masterarbeit selbständig und unter Beachtung der Regeln zur Sicherung guter wissenschaftlicher Praxis im Karlsruher Institut für Technologie (KIT) in der aktuellen Fassung angefertigt habe. Ich habe keine anderen als die angegebenen Quellen und Hilfsmittel benutzt und wörtlich oder inhaltlich übernommene Stellen als solche kenntlich gemacht.

_____

Tobias Kull

Acknowledgment

I would like to express my gratitude to everyone, who supported me during the realization of this work and during the entire time of my studies.

I want to thank Prof. Dr.-Ing. Marc Hiller, who made this work possible at the Institute of Electrical Engineering of the Karlsruhe Institute of Technology. I am sincerely grateful for the staff's support at the Project Competence E and I especially want to thank my supervisor M.Sc. Manuel Baena Martin, B.Eng. Ilhami Toklu and Dipl.-Ing. Nicolaus Lemmertz for their ongoing support and input.

Furthermore, I would like to thank Prof. Dr.-Ing Martin Gabi and Dra. Ing. Cecilia Smoglie who make the exchange program with the ITBA Buenos Aires possible and gave me the chance to participate in the double degree program.

Finally, I would like to express my profound gratitude to my parents, my family and my friends for providing me with support and continuous encouragement throughout my studies and throughout the process of writing this thesis. This would not have been possible without them. Thank you.

"Technology is the answer, but what was the question?"
-Cedric Price-

Abstract

The aim of this work was to develop a cell formation system for cycling and formation of lithium ion cells. The uniqueness of this system is the possibility of energy recuperation from the discharging process of the cell. Therefore, the hardware of an existing prototype was revised, and the corresponding firmware was developed. For the safe operation of the cell formation system, a battery management system was designed, and a high-level system control was realized in MATLAB. Together with an intermediate electrical storage, a cell formation unit for the formation and cycling of a lithium ion cell was commissioned. Subsequently, the system was characterized regarding the charging and discharging behavior and the efficiency in charging and discharging mode. Concluding, an economic evaluation was performed. The results suggest further development of the cell formation unit, as cost effectiveness is given depending on the choice of the intermediate electrical storage.

Kurzfassung

Das Ziel der vorliegenden Masterarbeit war es, eine Formiereinheit für die Zyklisierung und Formierung von Lithium-Ionen-Zellen zu entwickeln. Die Besonderheit dieser Formiereinheit liegt in der Möglichkeit der Energierückspeisung aus dem Entladevorgang der Lithium-Ionen-Zelle. Dazu wurde die Hardware eines bestehenden Prototyps der Formiereinheit überarbeitet und dessen Firmware programmiert. Zum Aufbau eines sicheren Teststandes wurde ein Batteriemanagementsystem entwickelt und eine übergeordnete Steuerung in MATLAB realisiert. Zusammen mit einem elektrischen Zwischenspeicher wurde ein Kanal zur Formierung/Zyklisierung einer Lithium Ionen Zelle in Betrieb genommen. Anschließend wurde das System bezüglich des Lade- und Entladeverhaltens und dessen Effizienz in Lade- und Entladebetrieb charakterisiert. Abschließend wurde eine Wirtschaftlichkeitsbetrachtung durchgeführt. Die Ergebnisse legen eine Weiterentwicklung der Formiereinheit nahe, da durch die Energierückspeisung je nach Wahl des elektrischen Zwischenspeichers ein wirtschaftlicher Vorteil beim Betrieb gegeben sein kann.

Resumen

El objetivo del presente trabajo ha sido el desarrollo de un sistema para formar y ciclar celdas de litio. La innovación principal de este sistema es la posibilidad de realizar una recuperación energética en el proceso de descarga de la celda de litio mediante un almacenamiento eléctrico intermedio. Ha sido necesaria una revisión hardware de un prototipo existente y la programación del firmware correspondiente para su correcto funcionamiento. Además, se ha desarrollado un sistema de gestión de batería para establecer un banco de pruebas, así como un control superior en MATLAB. También se ha realizado la puesta en marcha de un canal del sistema junto a un almacenamiento eléctrico intermedio. Posteriormente el sistema fue caracterizado respecto a su comportamiento y eficiencia en modo carga y descarga. Finalmente, se incluye una evaluación de rentabilidad que sugiere una continuación del desarrollo realizado en el presente proyecto, dado que la rentabilidad económica es viable dependiendo de la elección del almacenamiento eléctrico intermedio.

Table of Contents

Declaration of authorship III

Acknowledgment V

Abstract VI

Kurzfassung VI

Resumen VII

1 Introduction 1

2 Theoretical background 3

2.1 Lithium ion cells 3

2.1.1 Composition and operating principle of lithium ion cells 3

2.1.2 Production of Lithium ion cells 4

2.1.3 Operation of lithium-ion cells 6

2.1.4 Energy recuperation potential during formation and cycling 7

2.2 Power electronics 9

2.2.1 Buck Converter 9

2.2.2 Boost Converter 13

2.2.3 Synchronous converter 14

2.2.4 Current and voltage control 16

2.3 Levelized cost of storage and capital budgeting 18

3 Methods 21

3.1 Hardware 21

3.1.1 Cell formation system concept 21

3.1.2 Cell formation unit 22

3.1.3 Battery management system 24

3.1.4 Intermediate DC Storage 25

3.1.5 Laboratory Setup 25

3.2 Software development 27
3.2.1 Cell formation unit firmware 27
3.2.2 BMS firmware 30
3.2.3 PC software 31
3.3 Cycling and formation of cells 33
3.4 Electrical efficiency and energy recuperation 33
3.5 Economic Evaluation 36
4 Results and Discussion 39
4.1 Current and voltage control 39
4.2 Cycling of a LIP cell 41
4.3 Formation of a NMC cell 45
4.4 Electrical efficiency and energy recuperation 49
4.5 Economic evaluation 56
5 Conclusion and Outlook 58
References 59
Table of Figures 63
List of Tables 64
Listings 64
Appendix 65
A Schematics: cell formation unit 65
B Cell formation unit source code 70
C Intermediate DC storage 81
D Digital CD-R archive 83

1 Introduction

The transformation of the German energy system, away from fossil fuel combustion and towards renewable energy sources, comprises many technical, economic, and social challenges. One of these challenges is the need for sustainable and cost-efficient energy storage [1]. Stationary storage is needed due to the decoupling of energy demand and fluctuating energy generation from renewable sources. Future application fields are decentral PV-battery systems, optimization of own consumption and peak shaving, direct marketing of electricity and provision of balancing power [2]. Electric mobility is a driver for the development of energy storage with high gravimetric and volumetric density. Lithium ion batteries can fulfil a broad range of requirements for energy storage in stationary applications and electric mobility [2, 3]. The market situation of lithium ion batteries illustrates its potential: the global market volume in 2012 accounted for 748.2 million USD and is predicted to reach 16.6 billion USD by 2017 [4]. While the market was dominated by portable consumer electronics in the past, future applications will include traction batteries for electric mobility and stationary storage devices in the energy market. Increasing performance and decreasing production costs make lithium ion cells viable in these application fields. Compared to other battery types like nickel-metal hydride, nickel-cadmium or lead-acid batteries, lithium cells have a significant higher specific energy and specific power [5]. To further improve energy density, power density and lifetime and to lower production costs a considerable effort is made in material science research and research into industrial production processes [6–8]. One energy intense step of the lithium ion cell production is the cell formation. The cell formation consists of a series of charging and discharging procedures, which are necessary for the final conditioning of the cell. The formation can account for a considerable amount of energy consumption. Hence, this production step has a high potential to save energy and reduce production costs. Some of the commercially distributed cell formation systems are available with optional energy recuperation from the cell discharging [9, 10]. These systems use bidirectional AC/DC power converters. This can be a viable option for formation systems with high throughput, e.g. in commercial cell production facilities. With lower throughputs, for example in research facilities, the higher investment costs for a formation system including a DC/AC power inverter may not compensate for the reduced energy consumption. Therefore, another technology of energy recuperation must be found to implement a cost-efficient energy recuperation.

The aim of this thesis is to develop a cell formation system with the possibility of energy recuperation from the discharging process of the cell. In contrast to the commercially available solutions an intermediate stationary battery storage is used. Energy is drawn from the battery storage system for the formation and charging of the lithium ion cell. During the discharging of the lithium cell, the contained energy is fed back into the battery system. Conversion losses are compensated by recharging the intermediate battery system from the power grid. The bidirectional energy transfer between battery system and lithium ion cell is to be realized with a bidirectional DC/DC power converter.

In the beginning of this work, an overview over the necessary theoretical foundations will be given. First, a description of the lithium ion cell and its production process will be given. Furthermore, the basics of the power electronic circuits and the control system, that are used in this work, will be outlined. Also, two methods for the economic evaluation of the cell formation system are described. Subsequently, the development of the cell formation unit will be presented. Therefore, a detailed view on the hardware and software development is shown. The functionality of the system will be proved by cycling and formation of two different types of lithium ion cells. Additionally, the system will be evaluated regarding its electrical efficiency and its economic viability. Finally, an outlook on future working fields is given.

2 Theoretical background

In this chapter the theoretical background of the used methods is explained. In the first place, the composition, production, and charging/discharging behavior of lithium ion cells is outlined. The focus is set on the formation process of new cells and the theoretical energy recuperation potential is highlighted. Second, the fundamentals of the power electronic systems that are used in this thesis are explained. An overview over the necessary control system completes the power electronics chapter. Finally, two economic methods are described, which are used to assess the economic viability of the energy recuperation system.

2.1 Lithium ion cells

This chapter gives an overview of the composition, operating principle, and production of lithium ion cells with a focus on the cell formation. The typical operation and important parameters of lithium ion cells are described and the energy recovery potential is shown.

2.1.1 Composition and operating principle of lithium ion cells

The main components of a lithium ion cell are the positive and negative electrode, an electrolyte and a separator. There is a broad spectrum of cell chemistry, which defines volumetric and gravimetric energy density, nominal voltage, cost, capacity, safety and lifetime [11]. The anode active material is mostly made of graphite or amorphous carbon. The cathode is made of layered metal oxides, spinel-structured oxides or olivine-structured phosphates [12]. These materials allow lithium to be intercalated in the electrode material. Between the electrodes the cell is filled with electrolyte. The electrolyte is a lithium salt, mostly lithium hexafluorophosphate, dissolved in an organic solvent [13]. The lithium is dissolved into its ionic components which results in electrical conductivity of the solution. The separator is a porous membrane which is permeable for lithium ions but with ideally no electrical conductivity. It is realized as microporous polymer membranes, non-woven fabric mats or inorganic composite membranes [14]. On the surface of the negative electrode the solid electrolyte interface (SEI) is located. It is formed during the first charging process and acts as a protective layer between the electrode material and the electrolyte. In Figure 1 the basic structure of a lithium ion cell is shown. A lithium metal oxide is used as the material for the positive electrode. The negative electrodes active material is graphene.

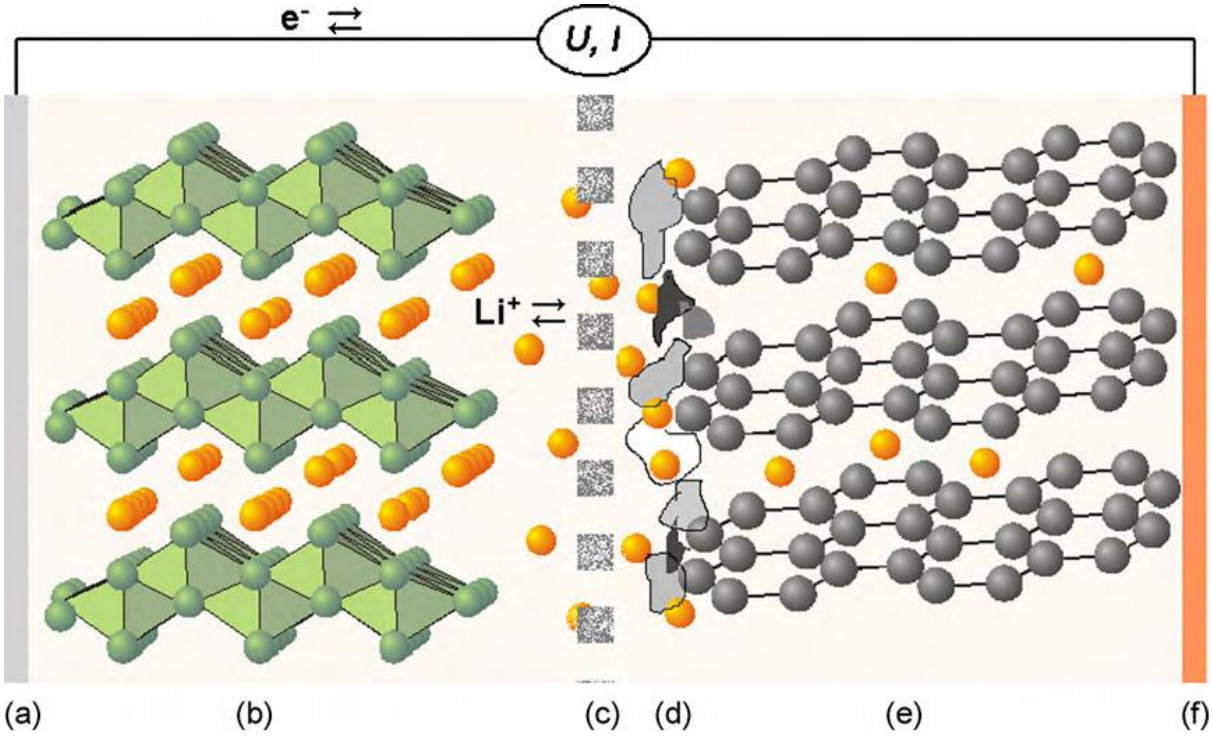

Figure 1: Illustration of a lithium ion cell: (a) aluminum current collector (positive electrode), (b) oxide active material, (c) porous separator, (d) solid-electrolyte interface, (e) graphite active material, (f) copper current collector (negative electrode) [15]

During discharging of the cell, electrons flow through the external circuit from the negative electrode (right side) to the positive electrode (left side). The electrical current is defined as the direction of positive charge carriers, so the electrical current flows from the positive electrode to the negative electrode. To sustain the charge equilibrium, positive lithium ions are deintercalated from the negative graphite electrode and move within the electrolyte to the positive electrode, where they are intercalated in the metal oxide structure. During charging of the cell the process is reversed. Electrons flow through the external circuit from the positive electrode to the negative electrode. Lithium ions are deintercalated from the positive electrode and move to the negative electrode, where they are intercalated in the electrodes' active material.

In this thesis two types of lithium ion cells are used: A lithium iron phosphate cell (LIP) is used for cycling and a nickel manganese cobalt oxide cell (NMC) is used for formation and cycling.

2.1.2 Production of Lithium ion cells

The production of lithium ion cells can be categorized in three main steps [11]: At first the electrodes are produced, then the cell is assembled and the last step of the cell production is the end-of-line conditioning. The production steps are explained below.

Production of electrodes

Initially the active materials, binders and additives are mixed and dispersed in organic solvents. The product of this process is called slurry. A thin film of the slurry is applied on current collector foils. Typically, aluminum is used for the positive electrode and copper is used for the negative electrode. The coated foils are dried to evaporate the solvents and achieve a porous electrode morphology. Then a calender is used to reduce and ensure a homogenous thickness of the coated foil. The electrode material is produced in a continuous process and winded on large coils.

Cell Assembly

After electrode production the cell is assembled. The first step of cell assembly is the slitting and cutting of the large electrode coils. In this step the size of the electrode material is reduced to the size of the cell. Afterwards the electrodes are dried again, and the further workflow takes place in a dry room. To produce pouch cells, the electrode sheets are stacked in alternating order of separator, anode, separator and cathode layers. To produce cylindrical or prismatic cells, winding technologies are applied. Then, the current collectors are joined and the cell is inserted into a cell housing. The last steps of cell assembly are the filling of the cell with the electrolyte and sealing of the cell housing. Lithium ion cells are assembled uncharged [11].

End-of-line conditioning

The first electrical cycles of the cell are called cell formation. Mainly during the first charging the SEI is formed [16]. As already mentioned, the SEI is a layer between the negative electrode and the electrolyte. It is formed from decomposition products of the electrolyte solvent and the solved lithium salt. The layer protects the cell from further electrolyte degradation during the operation of the cell. Ideally it has a high Li^+-ionic conductivity and a negligible electronic conductivity [17]. In subsequent cycles the morphology of the SEI can be matured [17, 18]. Depending on the cell chemistry and desired performance the cell formation can be done in different ways. For cheap consumer cells the formation may consist of only one partial charging process. The cell is not fully charged, but until the majority of the formation reactions are completed [11]. The voltage of the SEI formation onset varies from 0.8 to 2 V in the literature, but 0.8 V is a more frequently accepted value [15]. The production process must be well known and established to guarantee the desired cell properties without further electrical testing or cycling. This is why charging with two or more full charging/discharging cycles is a safer method regarding the identification and ensuring of the cell properties. The second cycle is hereby used as a quality control step [11]. Typically formation

currents are comparably low and in the order of magnitude of $C \leq 0.1\ h^{-1}$ (see Eq. 2-1) [19]. The exact formation protocols are core knowledge of the cell manufacturers, as this process significantly influences the properties of the cell. Materials, surface properties, formation current density, electrolyte additives, and cell temperature are important factors that influence the SEI formation [15, 17]. Because the formation is done with low currents, the duration can take up to two days, depending on the exact protocol. A considerable amount of energy is needed to charge the cell once or repeatedly.

The next step after formation is aging: To control the cell quality, it is stored a certain amount of time under controlled climatic conditions and the change of the open circuit voltage over time is documented. This way possible internal short circuits are detected and the self-discharge rate is determined [11]. Finally, more electrical testing can be done, e.g. electrochemical impedance spectroscopy or further capacity fading measurements.

2.1.3 Operation of lithium-ion cells

Lithium ion cells are commonly charged using a CC-CV-charging profile [4, 20]. At first the cell is charged with a constant current (CC) while the cell voltage increases steadily. After reaching a specified end-of-charge (EOC) voltage V_{eoc}, the cell is charged with a constant voltage (CV) which equals the end-of-charge voltage. During CV-charging the current decreases steadily. The charging process is completed either when a certain threshold current value I_{eoc} is reached, or after a specified CV-charging duration.

The nominal cell capacity Q_{nom} is given as electric charge in As or Ah with $1\ As = 1\ Coulomb$. Cell currents are often given as C rate. The C rate is the quotient of the cell current I and the nominal cell capacity Q_{nom} [4]:

$$C = \frac{I}{Q_{nom}};\ [C] = \frac{A}{As} = s^{-1} \qquad \textit{Eq. 2-1}$$

The C rate is often given in h^{-1}. A C rate of $C = 1\ h^{-1}$ means that the cell is fully charged in one hour. For a cell with a capacity of $Q_{nom} = 10\ Ah$ this equals a current of $I = 10\ A$. A C rate of $C = 0.1\ h^{-1}$ equals a current of $I = 1\ A$ and a charge duration of ten hours.

The state of charge (SoC) is the quotient between the capacity at a certain operating point $Q(V)$ and the nominal capacity Q_{nom}[4]. It is given in percent: A 100% state of charge equals the cell being fully charged, 0% state of charge equals the cell being fully discharged.

$$SoC(U) = \frac{Q(U)}{Q_{nom}} \qquad \textit{Eq. 2-2}$$

The depth of discharge (DoD) is the inverse value: A 100% depth of charge equals the cell being fully discharged, 0% depth of charge equals the cell being fully charged.

Lithium ion cells may not be operated outside of their specifications. Discharging under the specified end-of-discharge (EOD) voltage can lead to irreversible damages, e.g. capacity loss and increased self-discharge. Overcharging may lead to uncontrollable heating, thermal runaway and self-ignition [11, 21]. In order to avoid damage to the cell, a battery management system (BMS) should be implemented. The BMS surveils the cell current, cell voltage and cell temperature and breaks the circuit in case of exceeded specifications.

2.1.4 Energy recuperation potential during formation and cycling

The energy recuperation potential of the formation and cycling of cells is shown based on the current and voltage waveforms in Figure 2. It shows a typical formation protocol of a NMC lithium ion pouch cell. It has a nominal capacity of $Q_{nom} = 10\ Ah$. The formation is done with a commercially available cell test system (BaSyTec CTS) without energy recuperation [9]. During the first eleven hours and fifteen minutes the first charging takes place. Initially the cell is charged with a constant formation current of $I_{charge} = 900\ mA$. In this step the SEI is formed. When the end-of-charge voltage $V_{eoc} = 4200\ mV$ is reached, the cell is charged with a constant voltage and decreasing current. Afterwards the cell is discharged. Subsequently the cell is cycled twice with a higher charging current. Finally, the cell is charged partially for storage. Lithium ion cells should not be stored with low SoCs. Further self-discharging would lead to deep discharge and thereby damage to the cell [11]. To charge the cell energy is drawn from the grid. To discharge the cell the stored energy is converted into waste heat by an ohmic resistance. By integrating the charging and discharging power, the energy that is charged into the battery and discharged from the battery can be evaluated.

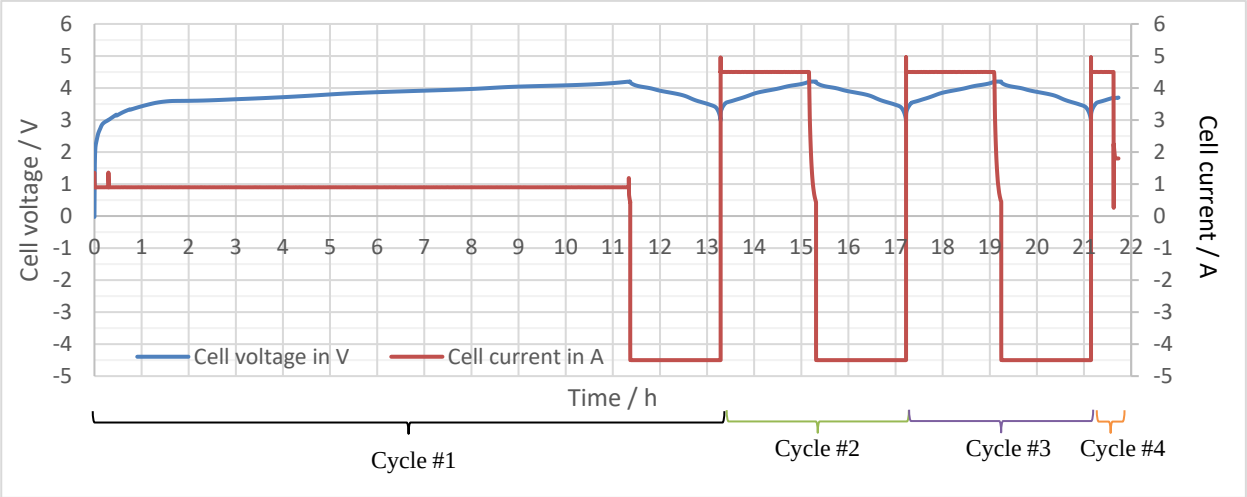

Figure 2: Cell formation of a 10 Ah lithium-ion pouch cell

Table 1 shows the charging energy of the cell, the discharging energy of the cell and the relative energy loss per cycle for the cycles one to four. The difference between the charging energy and discharging energy in the first cycle is -15.7%. The reason are endothermic reactions that take place during SEI formation and ohmic losses at the internal resistance of the cell during charging and discharging [17]. The energy loss in the second and third cycle is -3.3%. The losses in cycle two and three are mainly caused by ohmic losses at the internal resistance of the cell, but a small influence of chemical reactions within the cell cannot be ruled out [17].

Table 1: Charging energy, discharging energy and relative energy loss for cycle 1-4

E_{charge}	$E_{discharge}$	ΔE_{rel}
$E_{c,1} = 38.69Wh$	$E_{d,1} = 32.61Wh$	-15.7%
$E_{c,2} = 33.58Wh$	$E_{d,2} = 32.47Wh$	-3.3%
$E_{c,3} = 33.48Wh$	$E_{d,3} = 32.38Wh$	-3.3%
$E_{c,4} = 8.40Wh$		

With a device, capable of recuperating the energy of the discharging process the energy consumption can be reduced. As a result, the theoretical energy recuperation maximum of a formation cycle is 84.3% and the theoretical energy recuperation maximum of a charging/discharging cycle is 96.7%. The sum of the energy needed for charging is

$$E_{c,tot} = \sum_i E_{c,i} = 114.14\,Wh \qquad \text{Eq. 2-3}$$

and the sum of the energy that is converted into heat during discharging the cells is

$$E_{d,tot} = \sum_i E_{d,i} = 97.46\,Wh \qquad \textit{Eq. 2-4}$$

The theoretical maximum of energy recuperation of the complete protocol in Figure 2 is 85.38%. In other words, the energy consumption can be reduced to 14.62% compared to the original energy consumption without recuperation. This calculation is based only on the consumption and recuperation on cell level, the internal energy consumption and efficiency of the formation system is not considered.

2.2 Power electronics

Charging and discharging of lithium ion cells can be realized by means of power electronics. In order to charge and discharge cells with constant current and constant voltage from a storage battery a controlled DC/DC converter is needed. Buck and boost converters are a straightforward technology which reach high efficiency with comparably low system complexity [22]. They are direct forward converters and not galvanically isolated. In the following chapters, the basic function principles of both topologies and control systems are described. The concept is extended to a two-quadrant chopper. For the following contemplations all components are described with idealized behavior and semiconductor switches are operated in switching mode.

2.2.1 Buck Converter

The buck converter, or step-down chopper, is a DC/DC power converter using switching techniques. Figure 3 shows the circuit diagram of the buck converter. Its components are a switch S, a choke L, the diode D, and input and output capacitors C_1 and C_2. With this circuit a supply voltage V_1 is converted into a lower average output voltage V_2. The input and output voltages V_1 and V_2 are assumed to be constant in a first approximation when the system is in a steady state condition. Also, the ohmic resistance r_L of the inductor is neglected. This simplification is possible if $T/\tau_L < 0.05$ for a period T and the time constant $\tau_L = L/r_L$ with an inductance L. The resulting exponential waveform of the inductor current can then be regarded as linear [23].

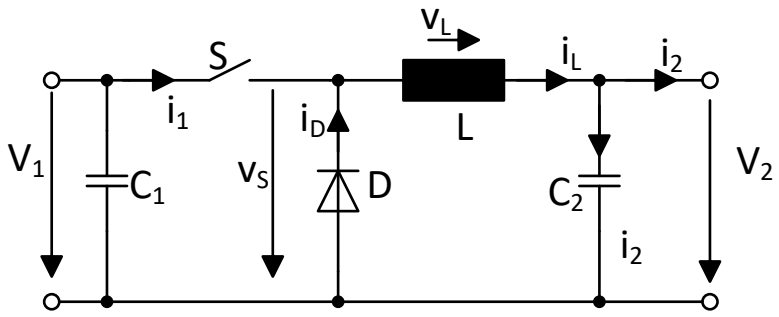

Figure 3: Schematics of the boost converter

The power conversion is done by periodically alternating the state of the switch S. During t_{on} the switch is on, and the voltage v_s equals the input voltage V_1. During t_{off} the switch is off and the voltage v_s is zero:

$$v_S(t) = \begin{cases} V_1 \; for \; t_{on} = t_1 - t_0 \\ 0 \; for \; t_{off} = t_2 - t_1 \end{cases} \qquad \textit{Eq. 2-5}$$

The proportion between on- and off-time of the switch is described by the duty cycle D.

$$D = \frac{t_{on}}{t_{on} + t_{off}} \qquad \textit{Eq. 2-6}$$

The sum of on- and off-time of the switch is the time period T, which defines the switching frequency f

$$T = t_{on} + t_{off} = 1/f \qquad \textit{Eq. 2-7}$$

The law of induction describes the inductor current i_L

$$v_L = L\frac{di_L}{dt} = v_S - V_2 \qquad \textit{Eq. 2-8}$$

During the on-time t_{on} of the switch S the inductor voltage is

$$v_L = L\frac{di_L}{dt} = V_1 - V_2 \qquad \textit{Eq. 2-9}$$

and the inductor current equals

$$i_L(t) = I_{Lm} + \frac{V_1 - V_2}{L}t \qquad \textit{Eq. 2-10}$$

With the minimum current value I_{Lm} at t_0

$$I_{Lm} = i_L(t_0 = 0)$$ *Eq. 2-11*

During the off-time t_{off} of the switch S the inductor voltage is

$$v_L = L\frac{di_L}{dt} = -V_2$$ *Eq. 2-12*

and the inductor current equals

$$i_L(t) = I_{LM} - \frac{V_2}{L}t$$ *Eq. 2-13*

with the maximum inductor current I_{LM}

$$I_{LM} = i_L(t = t_1) = I_{Lm} + \frac{V_1 - V_2}{L}t_1$$ *Eq. 2-14*

The average current I_2 is then

$$I_2 = \frac{I_{Lm} + I_{LM}}{2}.$$ *Eq. 2-15*

Figure 4 shows the alternating state of the switch S and the current waveform over time.

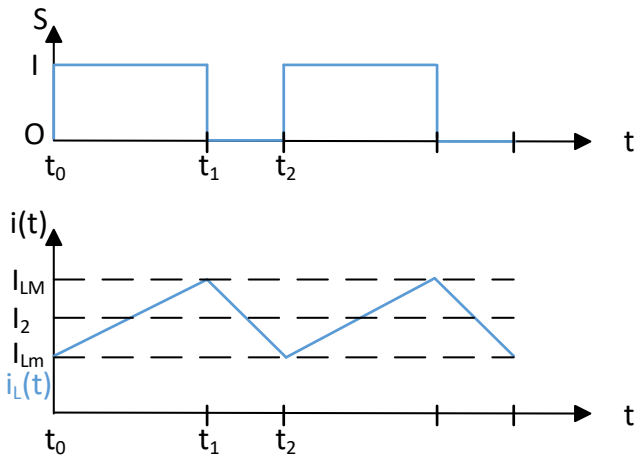

Figure 4: State of the switch S and choke current over time

In steady state conditions the net increase of the current is zero. By equating $i_L(t_0)$ with $i_L(t_2)$ the relationship between input and output voltage is dependent on the duty cycle D:

$$\frac{V_2}{V_1} = \frac{t_{on}}{t_{on} + t_{off}} = D \qquad \textit{Eq. 2-16}$$

The output voltage V_2 depends linearly on the duty cycle D. The current ripple can be calculated as

$$\Delta i_L = I_{LM} - I_{Lm} = \frac{TV_1}{L} D(1 - D) \qquad \textit{Eq. 2-17}$$

With a maximum at $D = 0.5$

$$\Delta i_{L,max} = \frac{TV_1}{L} \times 0.25 \qquad \textit{Eq. 2-18}$$

Figure 5 shows the normalized current ripple depending on the duty cycle D.

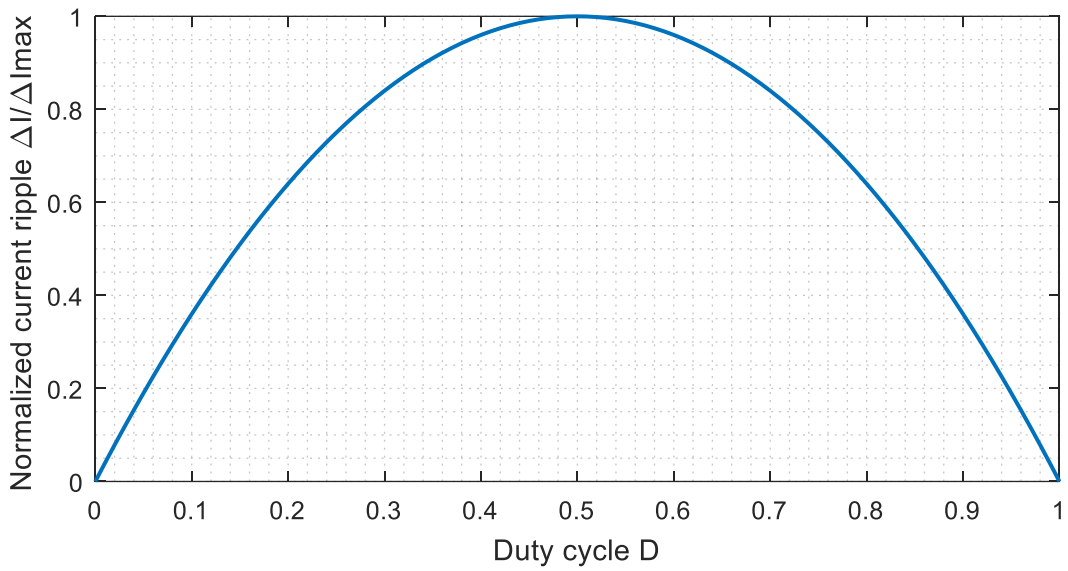

Figure 5: Normalized current ripple as a function of the duty cycle D

The buck converter can be operated in two modes: If the average inductor current is $I_L > \Delta i_L/2$ then the buck converter is operated in continuous conduction mode (CCM) and the current is always $i_L(t) > 0$. For $I_L < \Delta I_L/2$ the choke current is periodically zero. This mode is called discontinuous conduction mode (DCM) [24]. In DCM the relation between duty cycle and output voltage is nonlinear and depends on the load current. The current waveform after the zero-crossing is de-

scribed by a decaying oscillation [22]. The operation in discontinuous conduction mode can therefore also influence the stability of the control system. This problem can be solved in three ways: Parametrization of the control system according to the critical minimum load [24], operation only in continuous conduction mode, or replacement of the diode with a transistor to allow bidirectional current flow in the freewheeling path (see chapter 2.2.3). To charge a lithium ion cell from a 12 V battery, the input voltage is $V_1 = 12\,V$ and V_2 represents the cell voltage at the output. An ideal buck converter can theoretically reach an efficiency of 100%. In reality, losses are defined by the non-ideal behavior of the components. These are mainly switching and conduction losses of the transistor, the ohmic resistances of the choke and printed circuit board (PCB) traces, equivalent series resistance of the capacitor, switching and conduction losses of the diode, and static losses of the control and feedback circuit. Thus, the reduction of losses is mainly achievable by parameter optimization or reduction of the switching frequency. For an unchanged current ripple, the inductance of the choke then must be increased.

2.2.2 Boost Converter

The boost converter is a switched mode DC/DC converter which converts an input voltage V_1 into a higher output voltage V_2. Figure 6 shows the schematic of the boost converter.

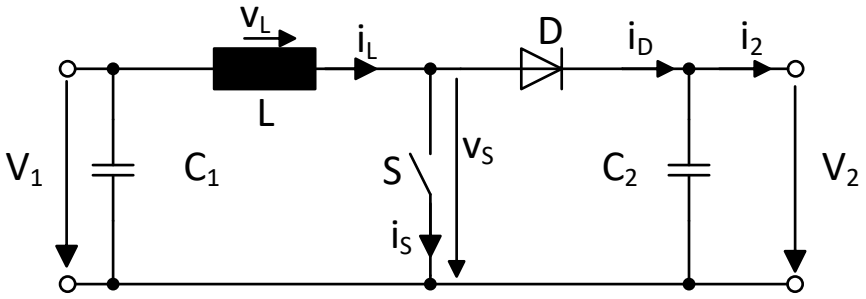

Figure 6: Schematics of the boost converter

Again, the input and output voltages V_1 and V_2 are assumed to be constant in a first approximation when the system is in a steady state condition. During t_{on} the switch is on, and the voltage v_s is zero. During t_{off} the switch is off, and the voltage v_s equals the output voltage V_2:

$$v_S = \begin{cases} 0\ for\ t_{on} = t_1 - t_0 \\ V_2\ for\ t_{off} = t_2 - t_1 \end{cases} \qquad \textit{Eq. 2-19}$$

The law of induction describes the inductor current i_L

$$v_L = L\frac{di_L}{dt} = V_1 - v_S \qquad \textit{Eq. 2-20}$$

During the on-time t_{on} of the switch S the inductor voltage is

$$v_L = L\frac{di_L}{dt} = V_1 \qquad \textit{Eq. 2-21}$$

and the inductor current equals

$$i_L(t) = I_{Lm} + \frac{V_1}{L}t \qquad \textit{Eq. 2-22}$$

with the minimum inductor current I_{Lm}. During the off-time t_{off} of the switch S the inductor voltage is

$$v_L = L\frac{di_L}{dt} = V_1 - V_2 \qquad \textit{Eq. 2-23}$$

And the inductor current

$$i_L(t) = I_{LM} + \frac{V_1 - V_2}{L}(t - t_1) \qquad \textit{Eq. 2-24}$$

with the maximum inductor current I_{LM}. With the steady state condition, a nonlinear dependence of the output voltage V_2 on the duty cycle D results.

$$\frac{V_2}{V_1} = \frac{1}{1 - D} \qquad \textit{Eq. 2-25}$$

The main difference to the buck converter is the nonlinear dependency of the output voltage V_2 on the duty cycle D. The losses of the boost converter are again defined by the non-ideal behavior of the real components. To discharge a lithium ion cell from a 12 V battery, the output voltage is $V_2 = 12\,V$ and V_1 represents the cell voltage at the input.

2.2.3 Synchronous converter

By combining buck and boost converter in a parallel coupling the inductance can be shared and both functions can be combined. The components of the equivalent buck converter are S_1, L and D_2. The components of the equivalent boost converter are S_2, L and D_1 (see Figure 7).

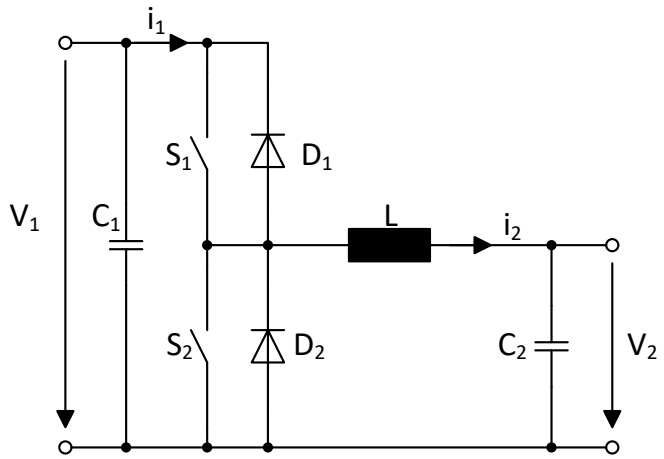

Figure 7: Synchronous converter schematics

The algebraic sign of the voltages V_1 and V_2 is the same, while current flow in buck and boost mode runs in opposite directions. This allows a bidirectional power flow in the output quadrants I and II (see Figure 8).

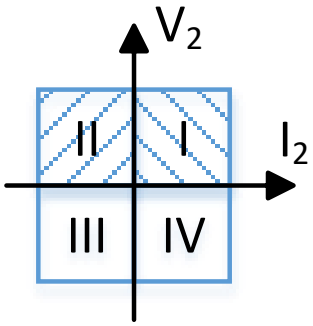

Figure 8: Bidirectional power flow in quadrant I + II (shaded area)

With this circuit the functionality of the diodes can be replaced by the paralleled switches to avoid the forward losses of the diode. The diodes are still needed though, as exact simultaneous switching is rarely achieved in the whole operating area. Still, losses can be reduced, if the conduction losses of the semiconductor switches are lower than the forward losses of the diodes. Also the reverse recovery losses of the diode can be avoided by short-circuiting the diode with the semiconductor switch [24]. Another advantage of the synchronous converter is the operating area of $I_2 < \Delta i_{max}$. While the buck converter is then operated in DCM, the synchronous converter allows bidirectional current flow.

2.2.4 Current and voltage control

The charging of lithium cells is done with a CC-CV charging profile (see chapter 2.1.3). Therefore, it is necessary to maintain a constant current or constant voltage at the output of the power converter by implementing a control system. Figure 9 shows the basic structure of a closed loop control system. A process variable $y(t)$ is measured and compared to a desired setpoint $w(t)$. The error $e(t)$ between the process variable and the setpoint is calculated and fed into the controller. The aim of the controller is to minimize the error $e(t)$ so that $y(t)$ equals $w(t)$ for any given point in time t [25]. The controller minimizes the error by adjusting the control variable $u(t)$ as the process variable $y(t)$ depends on the control variable $u(t)$ and the disturbance $d(t)$. In the case of constant voltage control $w(t)$ equals the desired charging voltage and $y(t)$ is the instantaneous charging voltage. In the case of current control, $w(t)$ is the desired charging/discharging current and $y(t)$ is the instantaneous charging/discharging current.

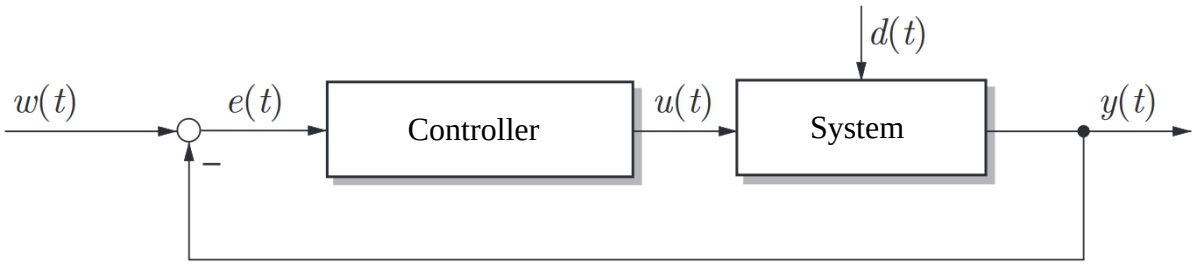

Figure 9: Basic structure of a closed loop control system [25]

For hard commutation converters like the buck and boost converter, usually the duty cycle of a pulse width modulation (PWM) with fixed frequency is used as control variable [26]. Based on PWM there are different ways to design the control loop: direct duty cycle control (DDC), voltage feedforward control (VFC) to consider changes of the input voltage, peak current mode control (CMC), and average Current Mode Control (CMC). DDC is the oldest and probably most widely used [22], and was also used in this work.

In many technical applications proportional-integral-derivative (PID) controllers are used as a control loop feedback mechanism [27]. It consists of three control terms. The proportional term

$$u(t) = k_p \times e(t) \qquad \textit{Eq. 2-26}$$

changes the control variable in a linear dependency on the error. With a proportional controller the deviation can be decreased fast, but not entirely, if the system itself does not show integral behavior. As a consequence, an integral term is added. The term integrates the error signal over time and reduces the steady state control deviation to zero.

$$u(t) = \frac{k_p}{T_I} \times \int_0^t e(\tau) d\tau \qquad \textit{Eq. 2-27}$$

A differential term is used to increase the speed of the transient response, increase damping, and decrease the overshoot:

$$u(t) = k_p T_D \frac{de(t)}{dt} \qquad \textit{Eq. 2-28}$$

However, the application of a differential term can lead to oscillations and instability of the control loop. The combined control function of the PID controller can be expressed as

$$u(t) = k_p \times e(t) + k_i \times \int_0^t e(\tau) d\tau + k_d \times \frac{de(t)}{dt} \qquad \textit{Eq. 2-29}$$

with

$$k_i = \frac{k_p}{T_i} \; and \; k_d = k_p T_d \qquad \textit{Eq. 2-30}$$

There are various methods to set the parameters k_p, k_i, and k_d. A commonly applied heuristic tuning method is the Ziegler-Nichols' closed loop method [25]: First, the control loop is closed with a proportional controller. The parameter k_p is increased until the system shows oscillations of constant frequency. The critical gain $k_{p,crit}$ and the period of the oscillation T_{crit} is used to calculate the parameters k_p, T_I and T_D according to Table 2. A requirement for this method is the ability of the system to oscillate without damage.

Table 2: Parametrization according to Ziegler and Nichols [25]

Controller	k_p	T_I	T_D
P	$0.5\ k_{crit}$		
PI	$0.45\ k_{crit}$	$0.85\ T_{crit}$	
PID	$0.6\ k_{crit}$	$0.5\ T_{crit}$	$0.12\ T_{crit}$

A PID controller can be improved by combining it with a feedforward control. More knowledge about the system is required, but in return, input variations can be processed better [25]. For the PID controller an inherent assumption is made [28]: opposed to the real-world system, the control algorithm has no limit of the process variable $u(t)$. If the real output shows nonlinear behavior in the form of a saturating element, integral windup can occur for large setpoint changes [29]. Consequences are a large overshoot in the step response and a high settling time. In this case the use of an anti-windup method is necessary. Possible methods are, amongst others, conditional integration, limited integration or anti-windup tracking [29]. Moreover, there is a broad range of other controller design methods, many of them including computer-aided modeling and simulation of the controlled system [30].

2.3 Levelized cost of storage and capital budgeting

To be able to assess the economic viability of the cell formation system, its cost structure must be regarded. The assessment can be divided in two tasks. At first a cost-efficient storage technology must be found. Second a cost comparison between a system I without energy recuperation and a system II with energy recuperation must be performed.

Fundamentally the total expenditure (TOTEX) can be divided in capital expenditure (CAPEX) and operation expenditure (OPEX) [31]. Expenditure differences between system I and system II will affect both, their CAPEX and OPEX. The CAPEX of both systems is comparably easy to assess as the components costs are known or can be taken from literature. The OPEX of system I is also comparably simple to assess, as energy from the grid is usually billed in €/kWh. In contrast, the OPEX of system II is more intricate: First, the energy needed from the power grid is reduced by the recuperation system and therefore dependent the efficiency of the cell formation unit and the exact cycling protocols. Second, the cost of the energy that is supplied from the 12 V storage battery depends on a variety of factors. The battery technology has the highest influence, as battery

technologies differ in cost per kWh, service life and cycle life. The cycle life again depends on the exact cycling protocols, as the applied DoD and C rates greatly influences the capacity fading of batteries [32, 33]. This means that also the capacity dimensioning of the storage battery is an important influencing factor.

A common method to evaluate costs of electricity is the levelized costs of electricity (LCOE) method, established by the international energy agency [34]. The key concept of the LCOE method is the comparison of the lifetime costs of an energy system with the total amount of produced energy. Initially developed as a method to compare technologies of power generation, it can be adapted to storage applications as levelized cost of storage (LCOS) [35]. The lifetime costs are composed of the initial CAPEX and the annual cost A_t of the storage system. The annual cost A_t is discounted with the interest rate i over the storage lifetime n. The sum of the system costs is divided by the annual energy production of the system. The discounting of the energy production can mislead, but it is a consequence of arithmetic operations [36].

$$LCOS = \frac{CAPEX + \sum_{t=1}^{t=n} \frac{A_t}{(1+i)^t}}{\sum_{t=1}^{t=n} \frac{W_{out}}{(1+i)^t}} \qquad \textit{Eq. 2-31}$$

The annual cost A_t consists of the annual operation cost $OPEX_t$, the annual reinvestments in storage system components $CAPEX_{re,t}$ and the cost of electricity supply for the storage. It is calculated from the product of the price c_{el} in €/kWh and the amount of annual electricity consumption W_{in}. Due to second use strategies a recovery value R_t can be included.

$$A_t = OPEX_t + CAPEX_{re,t} + c_{el} \times W_{in} - R_t \qquad \textit{Eq. 2-32}$$

Especially for lead-acid technology but also for other technologies the cycle life of a battery is dependent on the applied DoD. For lead-acid batteries, manufacturers usually guarantee a certain amount of cycles until the capacity is reduced to 60% of the nominal capacity. For lithium ion batteries the cycle life is given until the capacity is reduced to 80% of the nominal capacity. The energy output of the storage system is then calculated as the product of the average capacity over its lifetime C_{avg}, the number of cycles N and the cycling efficiency of the storage battery μ_{bat}

$$W_{out} = C_{avg} \times N \times \mu_{bat} \qquad \textit{Eq. 2-33}$$

Another circumstance that must be considered is the difference between the used net capacity C_{net} and the nominal capacity C_{nom} of the storage system as the cycle life of batteries depends on the applied DoD.

$$C_{net} = C_{nom} \times DoD \qquad \textit{Eq. 2-34}$$

The net capacity is not used directly in Eq. 2-31 but it is important for the capacity dimensioning of the storage. With the LCOS method the energy costs for the storage system can be calculated. Different storage technologies can be compared and the best technology can be chosen.

For a direct investment decision between system I and system II, or in other words the feasibility of a recuperation system, static or dynamic methods of capital budgeting must be used under consideration of all case specific constraints and boundary conditions. This can be the internal rate of return (IRR), net present value (NPV), equivalent annual cost (EAC), or the determination of the payback period and calculation of the break-even point [37]. As a general approach the static payback period is used in this thesis. The payback period of an investment object is defined as the period in which the used capital is recovered from the average returns or cash inflows of the object [38]:

$$payback\ period = \frac{used\ capital}{average\ returns} \qquad \textit{Eq. 2-35}$$

With these two methods, the LCOS and the static payback period, the economic viability of the cell formation system can be evaluated.

3 Methods

First, the development of the hardware setup is described in this chapter. The second part of the chapter outlines the development of software and firmware. Finally, cycling and formation of lithium ion cells are described and the economic methods are explained.

3.1 Hardware

In this chapter the development of the hardware components is described, beginning with the concept of the overall system architecture. Secondary, the testing of a existing prototype of the cell formation unit is outlined. A hardware revision, which was necessary due to hardware faults of the prototype, is documented. Furthermore, the development of a battery management system is described. Finally, the dimensioning of the 12 V storage and laboratory setup is shown.

3.1.1 Cell formation system concept

The general system architecture consists of eight cell formation units (Cellformer 1-8), each one containing a bidirectional DC/DC converter and microcontroller circuit for communication and individual current and voltage control. Every channel is independently monitored by the battery management system. This allows the formation and cycling of eight lithium ion cells independently at the same time. A laboratory PC running MATLAB is used for the overall system control. The communication is realized with a Controller Area Network (CAN bus). A common DC bus is used as a common power source for charging of the lithium cells and as a power sink for the discharging of the lithium cells. It is realized as a 12 V intermediate storage battery. Figure 10 shows a schematic of the system architecture. A detailed description of the components is given in the following chapters. In this work, one of eight channels was completed and is fully functional. The battery management system has eight working channels. The firmware of the cell formation units and battery management system is programmed for eight channels. The MATLAB software is programmed for one channel and is easily scalable for more than one channel.

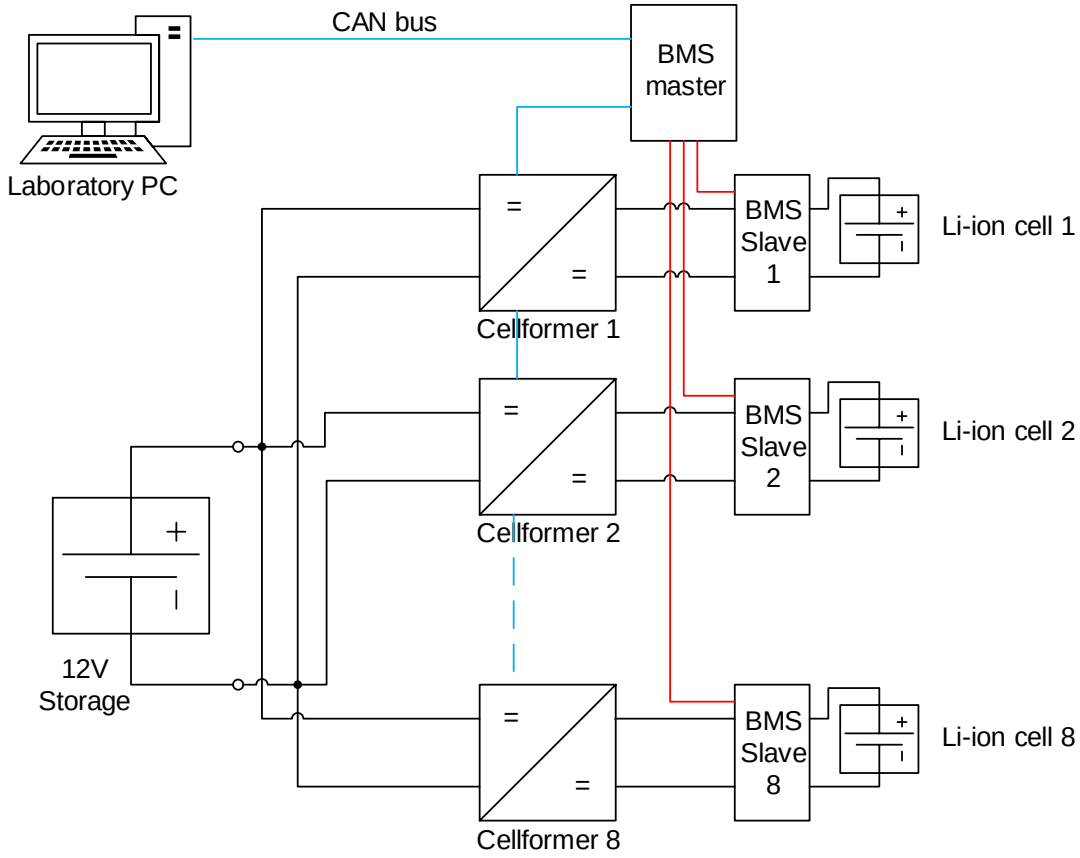

Figure 10: System architecture overview

3.1.2 Cell formation unit

A first hardware design of the cell formation unit had already been developed before the start of this thesis. Two prototypes had been manufactured. However, the prototype had not been tested and commissioned, and firmware still had to be developed. The cell formation unit was initially specified for cell currents of $I = [-10\ A,\ 10\ A]$ and cell voltages of $V = [0\ V, 4.3\ V]$.

The main functional units of the cell formation unit are a buck and boost converter realized with metal-oxide-semiconductor field-effect transistors (MOSFETs) and Schottky diodes. A 32-bit ARM Cortex-M4 based microcontroller from ST Microelectronics (STM32F405) is used for measurements and controlling. The cell current measurement is realized with a current shunt measurement and a hall sensor. Both, the cell voltage and intermediate storage voltage measurement are realized via voltage dividers. All values are digitalized by the integrated periphery 12-bit analog-digital-converters of the microcontroller. Communication with the host computer and BMS is provided via CAN bus. Programming and debugging is done via JTAG interface. The existing

concept provided a switching frequency of $f = 40\ kHz$ and a choke with $L = 400\ \mu H$. The fixed period of each duty cycle is therefore $T = 25\ \mu s$. The maximum current ripple is

$$\Delta i_{max} = \frac{12V \times 25\ \mu s}{4 \times 400\ \mu H} = 187.5\ mA \qquad \textit{Eq. 3-1}$$

During testing and commissioning the prototype, following hardware faults were found:

- Wrong supply voltage of the high side MOSFET driver circuit
- Current shunt measurement not connected to the microcontroller
- Hall sensor with inadequate accuracy and resolution
- PWM pins not connected to complementary timer outputs, thus no possibility for a two-quadrant chopper implementation
- Analog-digital-converters and PWM-outputs on the same port, which can lead to inaccurate measurements [39]

Due to these faults the cell formation unit was not functional and had to be modified. The hardware design was revised and eight revised cell formation units were needed. The new PCB was tested again and commissioned successfully. The schematics of the revised cell formation unit are documented in appendix A.

To be able to charge and discharge lithium ion cells in the specified operating area a constant current and constant voltage control had to be implemented. The control system is realized as direct duty cycle controlled PWM. The controller is a PI-controller and the parameters were tuned according to the Ziegler-Nichols' closed loop method (see chapter 2.2.4). This method was chosen based on the following contemplations: The input voltage is defined by the voltage of the 12 V battery. The input variation is within the specification of the battery and therefore limited. Furthermore, no quick input voltage changes are to be expected. Similar statements are applicable for the cell side: No abrupt load changes are to be expected and the dynamic requirements are low, regarding the long charging and discharging processes. Under these circumstances Ziegler-Nichols' closed loop method provides adequate results.

For the parametrization according to this method, it is necessary to increase the proportional gain until the system shows sustained oscillations (see chapter 2.2.4). This is not possible with a 12 V battery and a lithium ion cell, because the safe operating area for the batteries cannot be guaranteed. Therefore, the parameter tuning was done via load resistances. The load resistance values

were chosen in the range of the operating area of the cell, respectively the 12 V battery. For the parametrization of the buck converter current control a 12 V laboratory power supply was connected to the converter input and the load resistance was connected to the converter output. Two load resistances were used: $R = 0.01\ \Omega$ to simulate the beginning of the formation when the cell has a low voltage and $R = 2\ \Omega$ resulting in higher output voltages. For the parametrization of the buck converter voltage control two load resistances of $R = 2\ \Omega$ and $R = 10\ \Omega$ were used to map a broad spectrum of resulting currents. For the parameterization of the boost converter current control the cell formation hardware had to be modified: the control circuits (e.g. microcontroller and drivers) use the 12 V side for their power supply. Therefore, the buck converter output was split from the 12 V power supply for the control circuits, and a load resistance of $R = 10\ \Omega$ was connected to the converter output. A second power supply was used to simulate different cell voltages at the converter input. After the PID parameters were found, the control system was tested with a 12 V battery and a lithium ion cell. The parameters were tuned again manually to avoid overshoot and therefore guarantee operation of the cell within its specifications.

3.1.3 Battery management system

As already stated in chapter 2.1.3, charging and discharging of lithium ion cells beyond their specified voltage limits must be avoided under any circumstances. To avoid overcharging, deep discharge and overtemperature, a BMS was developed: Cell voltage and temperature of each channel are constantly monitored by the BMS. The battery management system was realized with a STM32F4Discovery evaluation board. It has an STM32F407 microcontroller and integrated periphery analog digital converters (ADC), which are used for measurements. The cell voltage is measured via voltage dividers and the cell temperature is obtained with a NTC thermistor. Only if the cell voltage and temperature are within the specified limits of the cell, a relay connects the positive electrode of the cell and the cell formation unit. The relay is driven by an independent 12 V voltage source. Minimum cell voltage, maximum cell voltage and cell temperature can be adjusted for every channel independently via CAN bus. If one of these values is surpassed, the safety relay opens. Moreover, a CAN message is sent to deactivate the cell formation unit and cancel the formation/cycling script execution in MATLAB (see 3.2.2). Figure 11 shows the schematics the battery management system with one channel depicted.

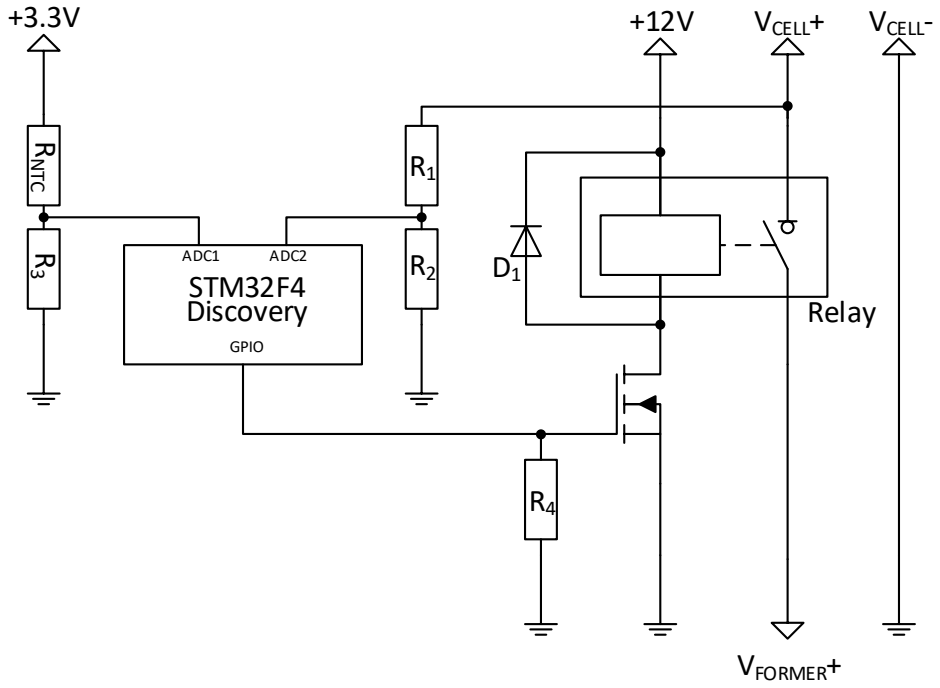

Figure 11: Battery management system schematic of one channel

A protection against overcurrent is realized via interchangeable fuses on the cell formation PCB. In a future revision it will be nonetheless advantageous to integrate the overcurrent protection into the battery management system. Additionally, it makes sense to increase the measurement accuracy by using external analog-digital-converters with higher resolution and take over the datalogging function from the cell formation unit (see chapter 3.2.1).

3.1.4 Intermediate DC Storage

A valve-regulated lead-acid battery with absorbent glass mat (VRLA-AGM) is used as a 12 V DC storage (see Appendix C for the datasheet). The electrolyte of a AGM battery is adsorbed in a glass mat. The advantages over conventional lead-acid batteries are lower self-discharging rate, no danger of acid leakage and valve sealing [40]. It has a capacity of 33 Ah and was chosen for initial measurements. Lead-acid battery technology is inexpensive compared to other battery technologies, and their low energy density is no disadvantage as the storage is stationary. For the final solution with eight cell formation units an economical assessment is performed (see chapter 4.5).

3.1.5 Laboratory Setup

Figure 12 shows the laboratory setup. The lithium ion pouch cell is mounted on a ceramic isolator plate. The power connectors for anode and cathode are realized with gold coated copper blocks. The current collectors of the cell are clamped into these blocks. The connectors have threaded

holes for cable lugs, connecting the cell to the battery management system. Additionally, they provide spring-loaded contacting for separate voltage measurements. Two temperature sensors, one for the cell formation system and one for the battery management system, are fixed on the surface of the cell.

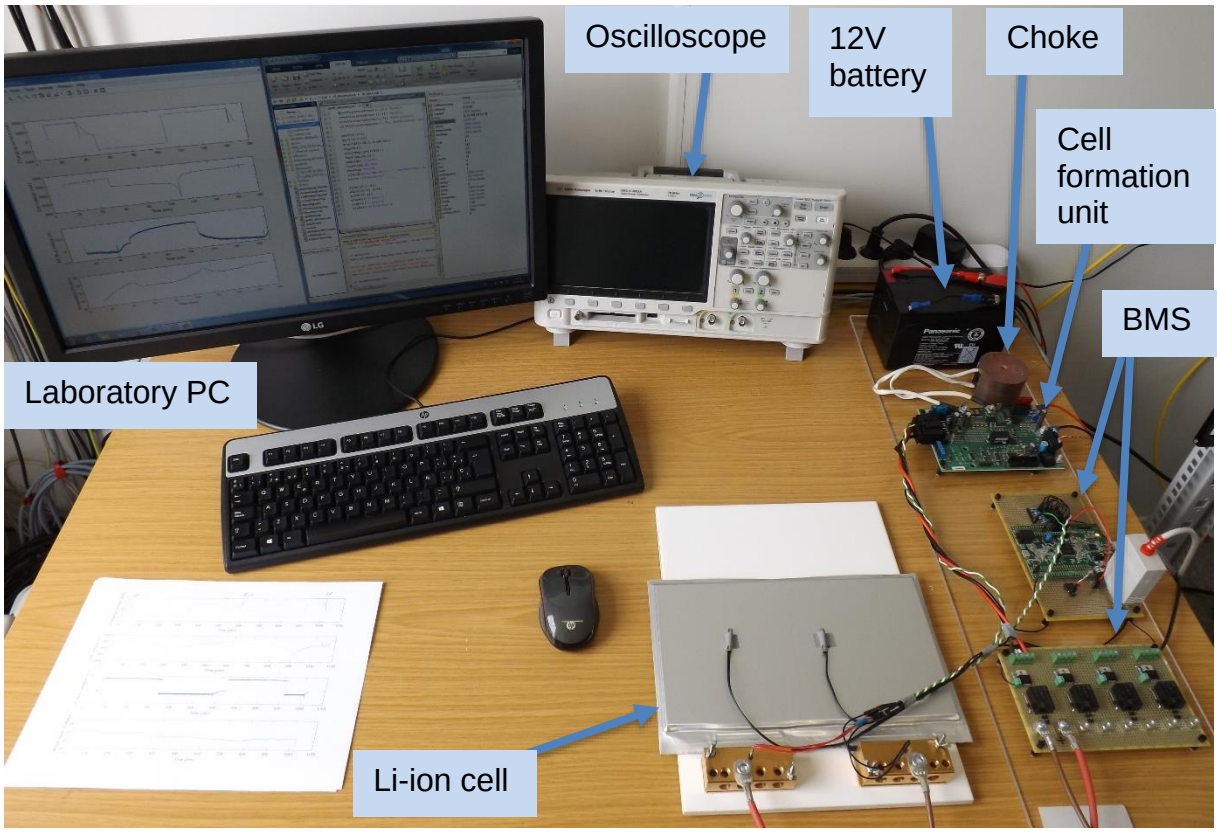

Figure 12: Laboratory setup for the formation of a 10 Ah lithium ion cell (NMC)

3.2 Software development

This chapter is focusing on the firmware development of the microcontroller, the firmware development of the battery management system, and finally the overall system control in MATLAB. The complete source code of microcontroller firmware, BMS firmware, MATLAB control scripts, and automated MATLAB evaluation scripts are included in the digital appendix D.

3.2.1 Cell formation unit firmware

The firmware of the microcontroller is programmed using the language C. For embedded real time systems, programming in C has various advantages: The language provides low-level access to the memory and periphery, the compiled code is fast and efficient, and only a minimal runtime support is required [41]. The code is written with an imperative and procedural approach and the controller functions are entirely interrupt-driven.

The core clock speed is $f = 144\ MHz$. Three 12-bit ADCs are used for cell current, cell voltage, DC storage voltage, and cell temperature measurements. These ADCs belong to the integrated periphery of the controller. They run with the maximum specified frequency of $f_{ADC} = 36\ MHz$. The cell current is measured continuously with the maximum specified sampling rate of 2.4 MS/s. All ADCs use direct memory access (DMA). This means the measurement results are written, once completed, directly into the memory of the controller. No processor core resources are needed for the measurements. The measurement resolution is $8\ mA\ /\ bit$ for the cell current and $1\ mV\ /\ bit$ for the cell voltage. Integrated peripheral hardware timers (TIM) are used for duty cycle control and CAN message timing. TIM1 is used to control the duty cycle of the buck and boost converter. It works with a frequency of $f_{TIM1} = 144\ MHz$. With a fixed switching frequency of $f_s = 40\ kHz$ the duty cycle resolution is therefor $40\ kHz/144\ MHz = 1/3600$. This means that the pulse width can be varied from 0 to 25 µs with a resolution of 6.94 ns. The PWM timer TIM1 is synchronized with the ADC measurement. It possesses complementary outputs with deadtime insertion, so there is a possibility to change from separated buck and boost converter mode to synchronous inverter mode in future revisions. The timer TIM2 is used for outgoing CAN message timing. Per default the cell formation unit sends the latest measurements in an interval of one second. This update rate can be changed in the PC software via CAN. The nested vectored interrupt controller (NVIC) is used to associate interrupt service routine (ISR) for PWM functions and incoming CAN messages.

The firmware is structured as follows: Coming from reset the general-purpose input/outputs (GPIOs), analog-to-digital converters, timers, direct memory access, controller area network and interrupt handler tables are configured and initialized and the controller enters an idle state. An incoming CAN message from the laboratory PC or the battery management system requests a CAN interrupt. The message is then evaluated in the associated interrupt service routine (CAN RX ISR). Depending on the content of the message, one of four modes is entered and the setpoint variables for the control algorithm are handed over. These modes are:

- Mode 0: Idle, no parameters
- Mode 1: CC-charging, charging current I_{charge}
- Mode 2: CV-charging: charging voltage V_{charge}
- Mode 3: CC-discharging: discharging current $I_{discharge}$

When entering mode 1) – 3) an ADC end-of-conversion interrupt is enabled. As already stated the ADC sample rate for the cell current is 2.4 MS/s and the measurement is synchronized with the PWM timer. This means 60 synchronized measurements are performed during each PWM period $T = 25\ \mu s$. The 60 values of the ADC are written via DMA into a double buffer array and an interrupt request is generated after each completion of one buffer. The associated interrupt service routine (ADC ISR) contains the control algorithm: The 60 values are averaged to eliminate the effect of the current ripple and calculate the arithmetic mean current value. This also leads to a constant sampling time for the PID controller. The averaged value is used in the control algorithm which sets the duty cycle output. The control algorithm also contains anti-windup by conditional integration and output clamping. The runtime of the control algorithm is about $t = 12.5\ \mu s$. This means that the measurement of a PWM period n is evaluated during period $n + 1$ and the duty cycle is set for period $n + 2$. Figure 13 illustrates the chronological order. The sampling is done by the ADCs with DMA without CPU resources. The averaging, PID control, and setting of the new duty cycle happens in the ADC ISR. The measurement values are sent via CAN in the CAN TX ISR.

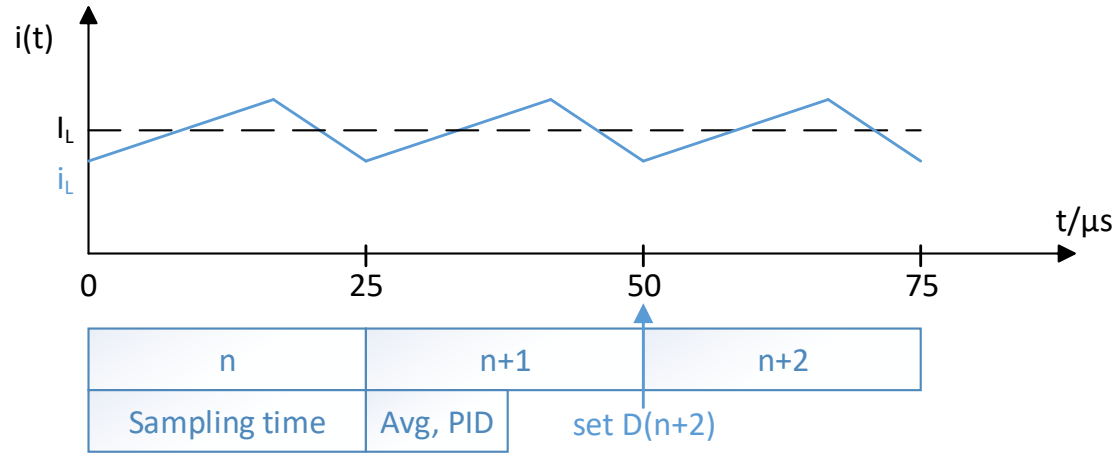

Figure 13: Schematic chronological order of measurement, control algorithm, and duty cycle set

The flowchart in Figure 14 illustrates the firmware structure of the cell formation unit. After configuration and initialization of the periphery, the runtime is defined by the CAN interrupt and the ADC conversion complete interrupt. The original source code can be found in appendix B.

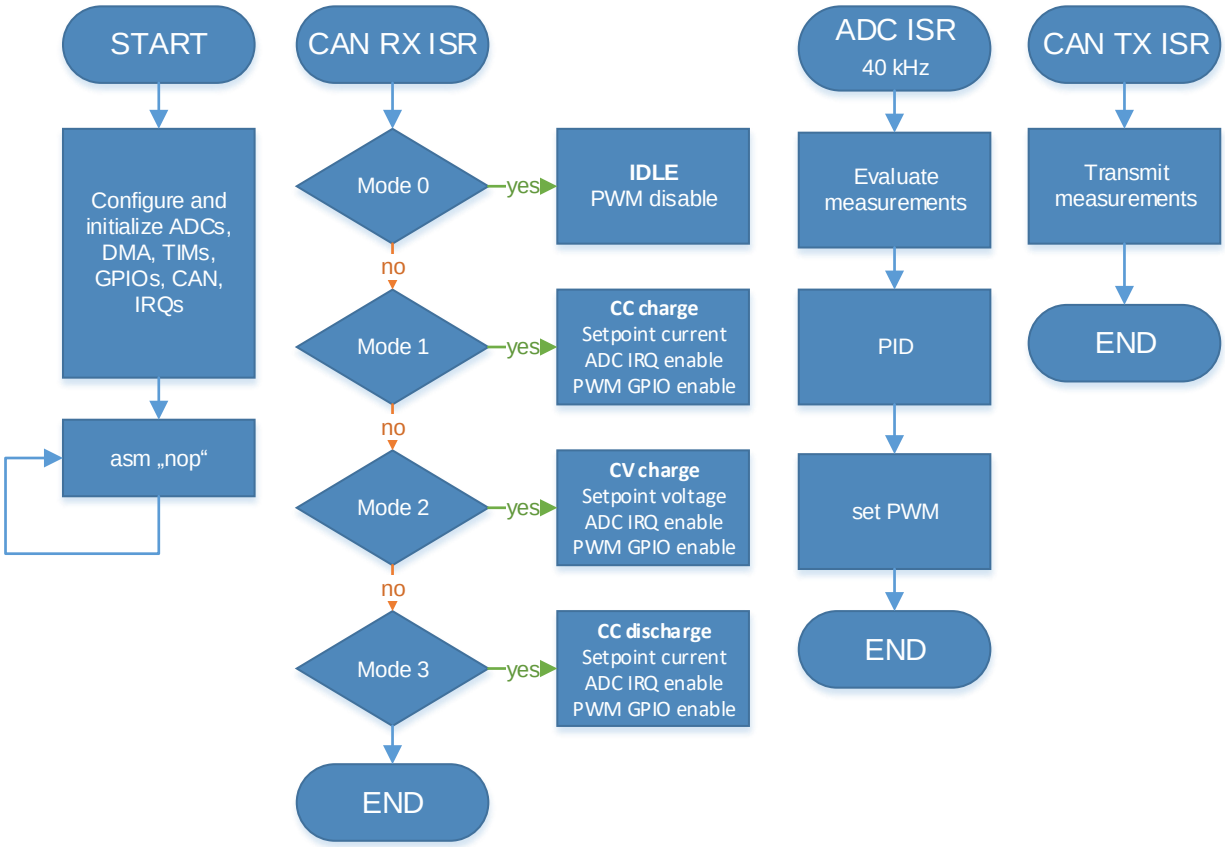

Figure 14: Cell formation unit firmware structure

3.2.2 BMS firmware

As already stated, the BMS was realized with a STM32F4Discovery evaluation board. The firmware is written in C. By default, the output pins are reset, so that the relays are normally open. Minimum and maximum cell voltages and maximum cell temperatures are received via CAN messages from the host PC. The cell voltages and cell temperatures of channel one to eight are constantly monitored. If the values are within their limits, the corresponding relay is closed. If the measured values exceed the limits the relays are opened. In case of an error (overvoltage, undervoltage or overtemperature) an error CAN message is sent. This is realized by checking the historical output status every cycle. The message sets the cell formation unit in idle mode and stops the execution of the MATLAB script, that is used for overall system control (see chapter 3.2.3). Furthermore, an error variable is transmitted, apprising the cause of the error. The output status of all eight channels is sent via CAN bus in an adjustable update rate (one second by default). It is transmitted as 8-bit binary integer variable. This way, every bit represents the status of one channel. Listing 1 shows a reduced source code example of the battery monitoring system written in C. The complete source code is included in the digital appendix D.

```
while(1)
{
  for(i=0;i<8;i++)
  {
    if(vcell[i]>=vcellmin[i] && vcell[i]<=vcellmax[i] && celltemp[i]<=celltempmax[i])
      {
        GPIO_SetBits(GPIOE, Output[i]);
        historic[i]=1;
      }
    else
      {
        GPIO_ResetBits(GPIOE, Output[i]);
         if(historic[i]==1)
           {
             //send CAN message to set cell formation unit idle and stop MATLAB script
             CAN_Transmit(CAN2, &TxMessage);
           }
         historic[i]=0;
      }
  }
}
```

Listing 1: Listing of the reduced BMS code in C

3.2.3 PC software

The overall control of the system is realized with a laboratory PC running MATLAB. The Vehicle Network Toolbox is used to provide connectivity to a PEAK-System CAN-USB interface. One script is used to control the battery management system and another script is used to control the cell formation unit. Both scripts are divided into a user editable section and a code execution section:

In the user editable section of the cell formation unit script $I_{charge,n}$, $V_{eoc,n}$, $V_{charge,n}$, $I_{eoc,n}$, $I_{discharge,n}$,$V_{eod,n}$ and $T_{cell,max,n}$ are defined for a desired number of cycles n. Running the script calculates the corresponding CAN messages and starts the cycling process depending on the values entered in the user editable section. During cell formation and cycling the incoming CAN messages from the cell formation unit containing the cell current, cell voltage, storage battery voltage and cell temperature measurements are logged. Additionally, the latest values are shown in a plot.

In the user editable section of the BMS script $T_{cell,max}$, $V_{cell,min}$ and $V_{cell,max}$ are defined for channel one to eight. Executing the script calculates the corresponding CAN messages and sends them to the battery management system. It can be called within the cell formation script, e.g. to change the minimum voltage after the formation cycle.

The basic code structure of the cell formation unit script is shown in Listing 2 (Pseudocode). The complete source code is included in the digital appendix D.

```
% USER EDITABLE SECTION
T_cell_max=40;
%First cycle
I_charge(1)=1000;
V_eoc(1)=4200;
V_charge(1)=4200;
...
%Second cycle
I_charge(2)=1000;
...

% CODE EXECUTION SECTION
for i=1:1:number_of_cycles

      send message IDLE-mode

      send message CC-CHARGE-mode
           while (V_cell <= V_eoc && T_cell < T_cell_max && V_storage >= V_storage_min)
                receive incoming CAN messages
                evaluate data
                log data
                plot latest values
           end

      send message IDLE-mode

      send message CV-CHARGE-mode
           while (I_cell >= I_eoc && T_cell < T_cell_max && V_storage >= V_storage_min)
                receive incoming CAN messages
                evaluate data
                log data
                plot latest values
           end

      send message IDLE-mode

      send message CC-DISCHARGE-mode
           while (V_cell >= V_eod && T_cell < T_cell_max && V_storage <= V_storage_max)
                receive incoming CAN messages
                evaluate data
                log data
                plot latest values
           end
end

send message IDLE-mode
pause(t)

%last logfile
while (t<timespan)
      receive incoming CAN messages
      evaluate data
      log data
      plot latest values
end
```

Listing 2: Pseudocode of the MATLAB control algorithm

3.3 Cycling and formation of cells

To show the functionality of the cell formation system a commercially available lithium ion cell (US26650FTC1) was cycled. It is a cylindrical cell of type 26650. The active material of this cell is lithium iron phosphate (LIP). It has a nominal cell voltage of $V = 3.2\ V$ and a nominal capacity of $Q_{nom} = 3000\ mAh$ at a C rate of $C = 0.2\ h^{-1}$. The end-of-charge voltage is $V = 3.6\ V$ and the minimum discharge cut-off voltage is $V = 2.0\ V$. For the cycling of the LIP cell a 12 V VRLA-AGM accumulator with a capacity of 33 Ah was used (see chapter 3.1.4). The accumulator is used as power source during charging of the LIP cell and used as a power sink during discharging of the LIP cell.

After the successful cycling of a LIP cell, a cell formation was done with a lithium ion pouch cell. This pouch cell is being actively developed and manufactured in the laboratory of KIT Competence E. The active material of the positive electrode is nickel-manganese-cobalt-oxide (NMC) and the active material of the negative electrode is graphite. The nominal capacity is $Q_{nom} = 10\ Ah$ and the nominal cell voltage is $V = 3.8\ V$. Despite the nominal capacity of 10 Ah the typical cell capacity is 9 Ah at the current state of research. The C Rates in chapter 4.3 therefore refer to a capacity of 9 Ah. Again, the power source and sink is a 12 V lead-acid accumulator.

3.4 Electrical efficiency and energy recuperation

The electrical efficiency of the cell formation unit was measured and evaluated in buck and boost mode. At a set of operating points the cell currents and cell voltages were measured. At the same time, voltage and current of the storage battery were measured. The efficiency measurements therefore refer to the efficiency of the power electronics including the microcontroller control circuits, but do not include the power consumption of the BMS or the laboratory PC. For the charging mode (buck converter) a laboratory power supply with a constant supply voltage $V_{source} = 12.5\ V$ was used at the cell formation unit input. For the simulation of different cell voltages and currents at the output, an adjustable electronic load was used. For the discharging mode (boost mode) the power supply was used to simulate the cell and the electronical load was used as a power sink with $V_{sink} = 12.5\ V$. When the cell formation system is operated with an intermediate battery storage, the voltage of the power source and sink depends on the SoC of the battery and will vary slightly. In this experiment, a variation of the storage battery voltage is neglected. The efficiency η_{charge}

for the charging mode (buck conversion) of the cell formation unit at every operating point is calculated as

$$\eta_{buck} = \left|\frac{i_{cell} \times v_{cell}}{i_{source} \times v_{source}}\right| = \left|\frac{p_{cell}}{p_{source}}\right| \quad \textit{Eq. 3-2}$$

with the battery storage acting as a power source. The instantaneous power consumption of the cell is

$$p_{cell} = i_{cell} \times v_{cell} \quad \textit{Eq. 3-3}$$

and the instantaneous power delivery of the battery is

$$p_{source} = i_{source} \times v_{source} \quad \textit{Eq. 3-4}$$

The total efficiency $\eta_{discharge}$ for the discharging mode (boost conversion) of the cell formation unit is calculated as

$$\eta_{boost} = \left|\frac{i_{sink} \times v_{sink}}{i_{cell} \times v_{cell}}\right| = \left|\frac{p_{sink}}{p_{cell}}\right| \quad \textit{Eq. 3-5}$$

with the storage battery acting as power sink and the instantaneous power consumption of the battery

$$p_{sink} = i_{sink} * v_{sink} \quad \textit{Eq. 3-6}$$

A linear surface fit to both measurement series was performed in MATLAB, which delivers interpolated efficiency values of the cell formation unit depending on cell current and cell voltage $\eta_{buck}(i_{cell}, v_{cell})$ and $\eta_{boost}(i_{cell}, v_{cell})$. These efficiency maps can be used to estimate the cycle efficiency of every formation or charging/discharging cycle. Only the cell voltage and current over time must be obtained to evaluate cycling efficiencies.

By integration over time, the total energy consumption of the cell for charging is calculated:

$$E_{cell} = \int_0^t p_{cell}(t)dt \quad \textit{Eq. 3-7}$$

Likewise, the energy that is delivered by the cell while discharging, can be calculated.

Via the efficiency maps the instantaneous battery storage power can be determined and the energy transfer from or to battery can be integrated. Therefore, the power of the storage battery is evaluated at the related operating point:

$$E_{source} = \int_0^t p_{source}(t)dt = -\int_0^t \frac{p_{cell}(t)}{\eta_{buck}(t)}dt \qquad \textit{Eq. 3-8}$$

and

$$E_{sink} = \int_0^t p_{sink}(t)dt = -\int_0^t \left(p_{cell}(t) \times \eta_{boost}(t)\right)dt \qquad \textit{Eq. 3-9}$$

The overall charging efficiency then is

$$\eta_{charge} = \left|\frac{E_{cell}}{E_{source}}\right| \qquad \textit{Eq. 3-10}$$

and the overall discharging efficiency is

$$\eta_{discharge} = \left|\frac{E_{sink}}{E_{cell}}\right| \qquad \textit{Eq. 3-11}$$

The cycle energy efficiency of one full cycle equals

$$\eta_{cycle} = \left|\frac{E_{sink}}{E_{source}}\right| \qquad \textit{Eq. 3-12}$$

With this method, the formation and cycling efficiency of a 10Ah NMC lithium-ion cell is calculated in chapter 4.4.

3.5 Economic Evaluation

As explained in chapter 2.3, the LCOS method can be applied to determine the best storage system for the energy recuperation regarding cost. Two different storage technologies were compared, and two representative examples per storage technology were evaluated. First, two VRLA-AGM batteries are considered, one with a capacity of 35 Ah, which requires one battery per cell formation unit, and another one with a capacity of 260 Ah as shared storage for eight cell formation units. Furthermore, LIP batteries are considered as intermediate storage. These batteries have a higher price *P* per Ah, but therefore provide a higher cycle life at a higher DoD, so that the capacity can be dimensioned smaller.

For the calculation of the LCOS some assumptions are made. The different storage technologies provide diverse cycle life, so that the evaluation must be referred to a representative benchmark case. This benchmark case was defined by a certain amount of formation and cycling processes per year using an exemplary cell type and considering the efficiency of the cell formation unit. For the benchmark case the formation protocol from Figure 2 in chapter 2.1.4 is used. The number of formations per year and channel is limited to a maximum of 403 due to its duration of 22.75 h. Regarding the set-up time and limited number of work days per year, a number of 250 formations per year and channel is reasonable. This equals 2000 formations per year using all eight units. The efficiency of the cell formation unit was included with the methodology of chapter 3.4. For the discount rate a weighted average cost of capital (WACC) of 8% was assumed and the service life was set to 10 years. These parameters can of course vary depending on the specific investment case. Because all batteries are maintenance free, the annual $OPEX_t$ was assumed as zero. The reinvestment $CAPEX_{re,t}$ depends on the cycle life of each specific battery type, the VRLA-AGM batteries have to be replaced earlier than the LIP batteries due to their inferior cycle life. The lead acid battery end-of-life (EOL) is reached when the capacity is faded to 60% of the nominal capacity. The LIP EOL is reached when the capacity is faded to 80% of the nominal capacity as specified by the manufacturer. As a consequence, the lifetime cannot be directly compared. This shortcoming can be compensated by the assumption of a higher recovery value R_t for the LIP technology. The recovery value was calculated as

$$R_t = P \times \frac{residual\ cycle\ life}{cycle\ life} \times g \qquad \textit{Eq. 3-13}$$

with a compensation factor g. The electricity generation price was assumed as zero, because the energy recuperation is essentially a free energy source. The necessary CAPEX for the energy recuperation system are taken into account in the capital budgeting method. Table 3 shows a parameter overview of the examined storage batteries.

Table 3: Parameter overview of selected battery types for intermediate storage [42–45]

Type	C_{nom}	*DoD*	C_{net}	*p*	C_{EOL}	C_{avg}	*Cycle life*
Siga S35-12 AGM, Pb	35 Ah	0.3	10.5 Ah	84 €	0.6 $Cnom$	0.85 Ah	1500
Siga S260-12 AGM, Pb	260 Ah	0.3	78 Ah	469.5 €	0.6 $Cnom$	0.85 Ah	1500
Super B SB12V100E, LIP	100 Ah	0.8	80 Ah	1,899 €	0.8 $Cnom$	0.95 Ah	5000
Victron Energy BMS, LIP	160 Ah	0.5	80 Ah	2,437 €	0.8 $Cnom$	0.95 Ah	10000

To answer the question if the cell formation system with energy recuperation is economically viable over the system without energy recuperation, a static payback period analysis was performed (see Eq. 2-35).

In the case of system II the used capital is the additional cost for the energy recuperation components. The average returns are the saved energy costs. Additionally, cooling costs can be considered, as the cell's discharging energy must be dissipated if no recuperation system is implemented. The same benchmark case as for the LCOS calculation was used. For a comparison with grid energy prices, data from the German Association of Energy and Water Industries (BDEW) was used. The BDEW performs periodic electricity price analysis for households and industrial consumers on a regular basis. The 2017 price of electricity taken from this analysis is valid for industrial medium voltage level consumers with a yearly consumption of over 160,000 kWh and amounts to 17,02 ct/kWh [46]. The cost of the Cellformers for system I and II were estimated as equal as the discharging technology does not matter. The implementation of a power electronic circuit for cell discharging with power resistors will likely compensate the omitted boost converter. The energy costs are evaluated in chapter 4. Table 4 shows an overview of the relevant component costs for the payback period calculation.

Table 4: Overview of the relevant component costs for the payback period calculation

Component	*Quantity*	*Type*	*Price per unit*	*System*
Cellformer I	8	$CAPEX$	274.08 €	I
Cellformer II	8	$CAPEX$	274.08 €	II
Choke	8	$CAPEX$	58.06 €	$I + II$
Load resistance	8	$CAPEX$	6.40 €	I
Energy cost I	$per\ kWh$	$OPEX$	17.02 ct	I
Energy cost II	$per\ kWh$	$OPEX$	$see\ chapter$ 4.4	I
Cooling cost	$per\ kWh\ heat$	$OPEX$	$see\ chapter$ 4.5	I

4 Results and Discussion

In the following chapter the functionality and viability of the cell formation system will be shown in different aspects. Primarily the characteristics of the current and voltage control will be presented. Subsequently the cycling of a LIP cell and the formation of a NMC cell is documented. The electrical efficiency in the operating area of buck and boost converter is evaluated, and the cycle efficiency for a formation cycle and a charging cycle is shown. Finally, the results of the economic viability assessment of the cell formation system are presented.

4.1 Current and voltage control

The dynamic properties of the control system can be evaluated by regarding the step response of the closed control loop to a given setpoint change. In a first measurement the step response of the current control in buck mode (charging the lithium ion cell) is shown. The input of the buck converter is connected to the 12 V battery and the output is connected to a 10 Ah NMC lithium ion cell with a cell voltage of $V_{cell} = 3.8\,V$. Figure 15 shows the step response $y(t) = i(t)$ of the closed loop with a setpoint change of $w(t) = I_c * \sigma(t)$, where I_C is the charging current of 5 A. The zero point on the timescale is defined as the moment of the transistor's first switching. This way deadtime coming from the microcontroller (e.g. CAN evaluation runtime) is ignored. A 95 % of the setpoint value is reached after 5.55 ms. A 99.3% of the setpoint value is reached after 9.1 ms.

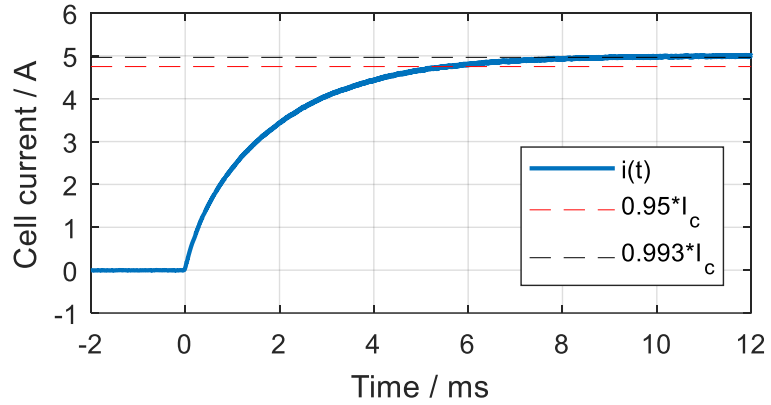

Figure 15: Step response of the closed loop current control in buck mode (charging)

In a second measurement the step response of the current control in boost mode (discharging the lithium ion cell) is shown. The input of the boost converter is connected to a 10 Ah NMC lithium ion cell with a cell voltage of $V_{cell} = 3.8\,V$ and the output is connected to the 12 V storage battery. Figure 16 shows the step response $y(t) = i(t)$ of the closed loop in boost mode (discharging the lithium ion cell) with a setpoint change of $w(t) = I_d \times \sigma(t)$ where I_d is the discharging current

of -5 A. A 95 % of the setpoint value is reached after 133.3 ms. A 99.3% of the setpoint value is reached after 153.5 ms. Contrary to the buck mode, the boost mode step response shows deadtime behavior. The reason is the operation of the boost converter against the imposed voltage of the storage battery.

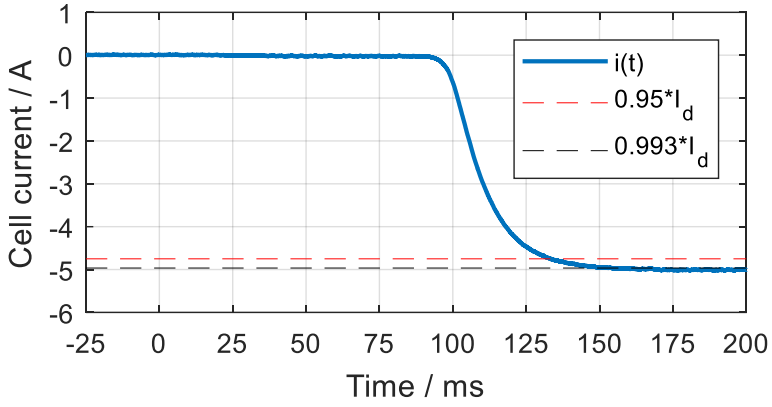

Figure 16: Step response of the closed loop current control in boost mode (discharging)

In both cases, the current control shows stationary accuracy and a fast settling time without overshoot.

Voltage control is used to keep the end-of-charge voltage constant at the end of a CC-phase and is only used for charging the cell (buck mode). Applying a voltage setpoint that does not equal the cell voltage would either lead to a very high inrush current if the cell voltage was lower than the setpoint voltage, or to zero current if the cell voltage was higher than the setpoint voltage. For this reason, the functionality of the voltage control is shown with the 12 V battery at the input of the buck converter and a load resistance at the output of the buck converter. Figure 17 shows the step response $y(t) = v(t)$ of the closed loop voltage control in buck mode with a load resistance of $R = 2\Omega$ at the converter output and a setpoint change of $w(t) = V_c \times \sigma(t)$ where V_c is the charging voltage 4200 mV. A 95 % of the setpoint value is reached after 48.3 ms. A 99.3% of the setpoint value is reached after 77.2 ms. The value of the resistor was chosen to simulate a typical operation point of the CV-control. The resulting load current of $I = 2.1A$ is within the typical current range for the CV-phase during formation and cycling (see chapter 4.2 and 4.3). The functionality of the voltage control is further shown implicitly by a constant current charging followed by a constant voltage charging in the following chapter.

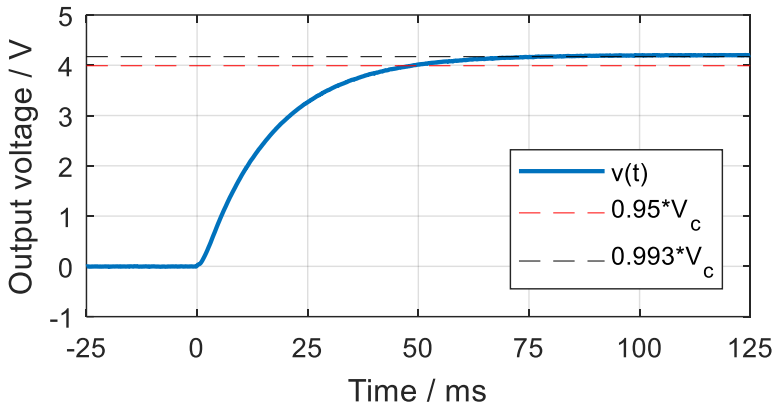

Figure 17:Step response of the closed loop voltage control in buck mode (charging)

4.2 Cycling of a LIP cell

After the control system was configured, a cylindric lithium iron phosphate cell was charged and discharged with CC- and CV-profiles (for cell specifications see chapter 3.3). Table 5 shows the chronological cycling protocol with mode, setpoint, and the termination criterion.

Table 5: LIP cell cycling protocol

Mode	Setpoint	Termination criterion
CC-discharging	$I_{cell} = -3000\ \mathrm{m}A\ (C = -1\ h^{-1})$	$V_{eod} = 2100\ mV$
CC-charging	$I_{cell} = 1500\ \mathrm{m}A\ (C = 0.5\ h^{-1})$	$V_{eoc} = 3600\ mV$
CV-charging	$V_{cell} = 3600\ \mathrm{m}V$	$I_{eoc} = 100\ mA$
CC-discharging	$I_{cell} = -3000\ \mathrm{m}A\ (C = -1\ h^{-1})$	$V_{eod} = 2100\ mV$

Figure 18 shows the LIP cell voltage over time and Figure 19 shows the LIP cell current over time. Initially the cell has about 20% SoC and the CC-discharging begins at $t = 0$. After 11 minutes and 49 seconds the end-of-discharge voltage V_{eod} is reached and the cell is fully discharged (0% SoC.) At this point, the CC-charging begins. The voltage increases steeply in the first minutes. Between $t = 20\ min$ and $t = 115\ min$ a pronounced voltage plateau can be observed. This is the typical behavior of lithium iron phosphate cells. After 123 minutes and 41 seconds the end-of-charge voltage is reached, and the CV-charging begins. The cell voltage is constant and the cell current decreases steadily with time. When the current falls below the termination criterion of $I_{eoc} = 100\ mA$ the CV-phase ends. This is the case after 130 minutes and 50 seconds. A CC-discharging

is done with a cell current of 1500mA. Again, the typical voltage plateau can be seen while discharging. When the termination criterion $V_{eod} = 2.1\ V$ is reached (188 minutes and 5 seconds) the cell is fully discharged. The capacity of the cell can be calculated by multiplying the discharging current and the duration of the second CC-discharging:

$$Q = 0{,}9542\ h \times 3000\ mA = 2862{,}6\ mAh \qquad \textit{Eq. 4-1}$$

The calculated capacity is lower than $Q_{nom} = 3000mAh$. The reason is the dependency of the capacity on the discharging current. Q_{nom} is specified for $C = -0.2\ h^{-1}$ and the used discharging current was $C = -1\ h^{-1}$. The higher discharging current leads to a lower capacity.

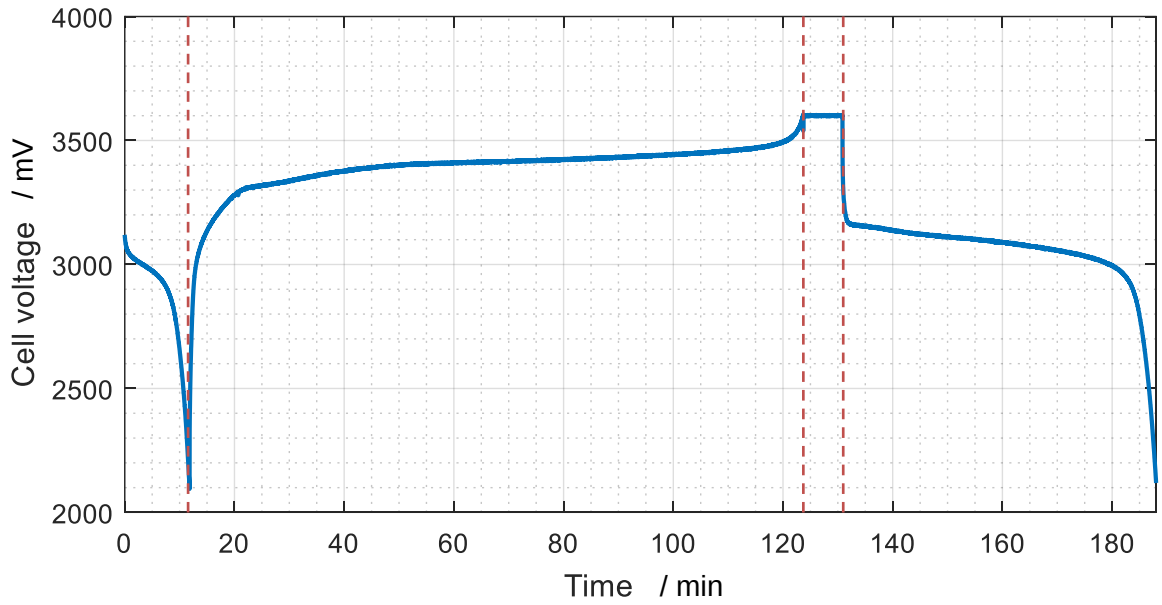

Figure 18: Cell voltage of lithium-iron-phosphate cell over time

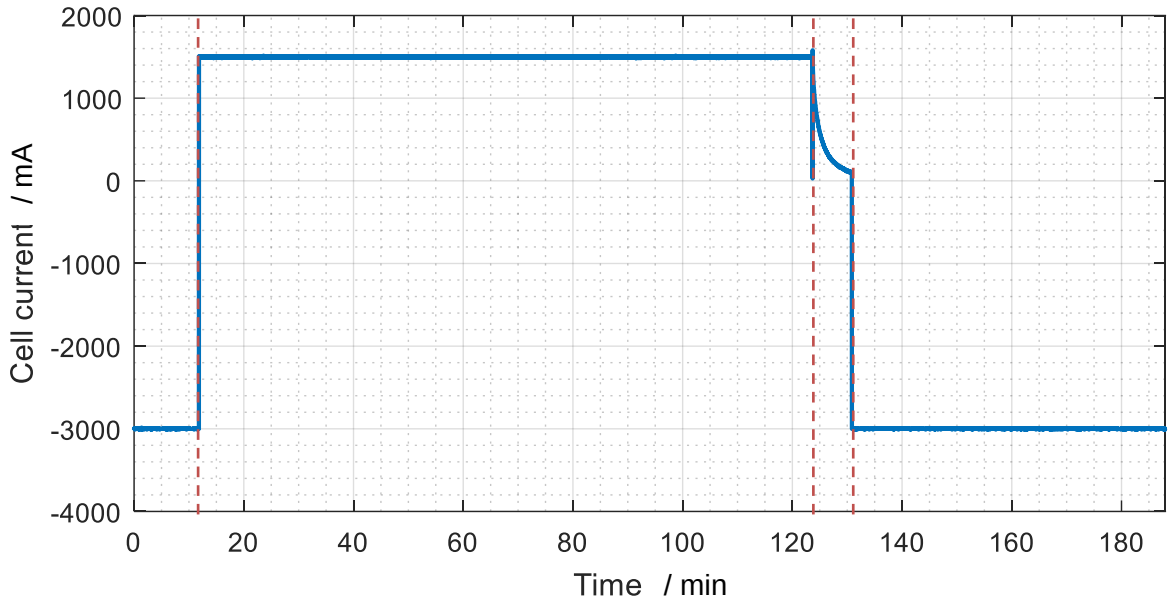

Figure 19: Cell current of the lithium iron phosphate cell over time

Figure 20 shows the voltage of the 12 V lead-acid battery which is used as power source and sink. While discharging the LIP cell the storage battery is charged, and the voltage increases. Charging of the LIP cell causes a decrease in the lead-acid battery voltage, as energy is drawn from the battery. Figure 21 shows the cell temperature over time. During discharging the temperature increases from 18°C up to 21°C. The increase in temperature is caused by ohmic losses of the internal resistance of the LIP cell. During charging, the temperature decreases initially down to 19.3°C and then increases up to 21.6°C. Losses are linearly dependent on the internal resistance and quadratically dependent on the current. Additionally, the internal resistance is linearly dependent on the current. As the charging current is lower than the discharging current, the losses during charging are lower, resulting in a lower temperature increase. This can be observed again during the last discharging, as the temperature increases again up to 24.5°C.

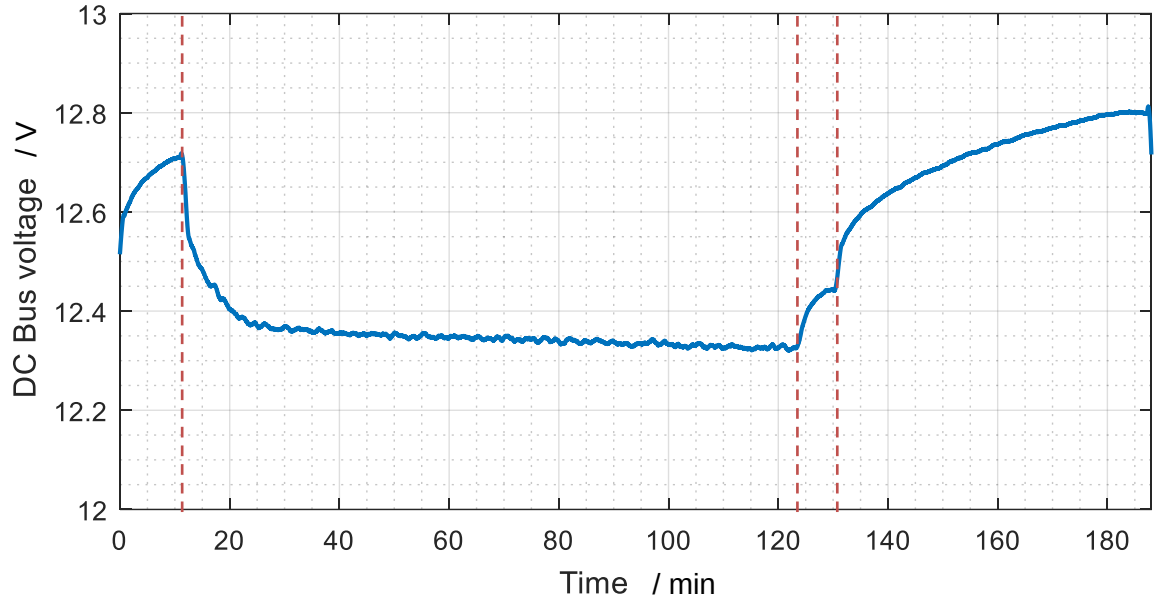

Figure 20:Voltage of the 12V DC-bus lead acid battery over time

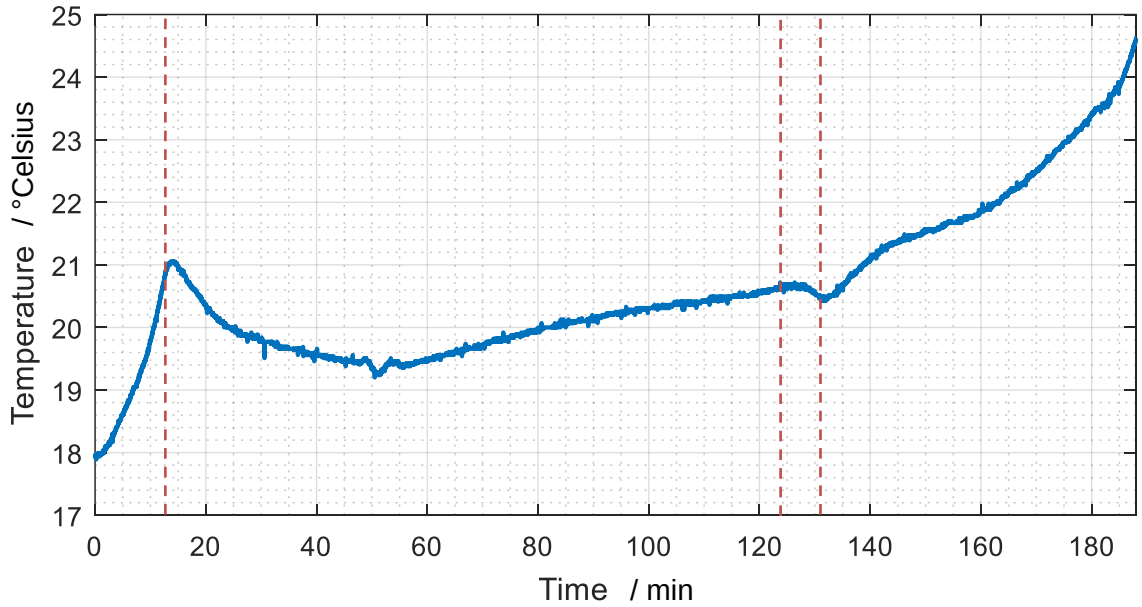

Figure 21: Temperature of lithium-iron-phosphate cell over time

Hence, the developed cell formation system is capable of cycling lithium ion cells with energy recuperation during cell discharge. The cell current, cell voltage, cell temperature, and the voltage of the storage battery are measured by the cell formation unit and logged in MATLAB. In the next chapter a cell formation of a NMC cell is shown.

4.3 Formation of a NMC cell

After the successful cycling of a LIP cell, the formation of a NMC pouch cell was done (for cell specifications see chapter 3.3). The first formation charging was done with a CC-phase of $C = 0.1\ h^{-1}$ and an ensuing CV-charging with $V_{eoc} = 4200\ mV$. During the first CC-charging, most of the SEI-building reactions take place. After discharging, the cell was subsequently cycled twice with a CC- and CV-charging and CC-discharging. The full charging protocol is shown in Table 6. Note that the C rates are based on the typical capacity of $Q = 9\ Ah$, not the nominal capacity $Q_{nom} = 10\ Ah$ (see chapter 3.3).

Table 6: Protocol of the formation and cycling of a 10 Ah NMC cell

Mode	Setpoint	Termination criterion
CC-charging	$I = 900\ mA\ (C = 0.1\ h^{-1})$	$V_{eoc} = 4200\ V$
CV-charging	$V = 4200\ mV$	$I_{eoc} = 150\ mA$
CC-discharging	$I = -4500\ mA\ (C = -0.5\ h^{-1})$	$V_{eod} = 3000\ V$
CC-charging	$I = 4500\ mA\ (C = 0.1\ h^{-1})$	$V_{eoc} = 4200\ V$
CV-charging	$V = 4200\ mV$	$I_{eoc} = 200\ mA$
CC-discharging	$I = -4500\ mA\ (C = -0.5\ h^{-1})$	$V_{eod} = 3000\ V$
CC-charging	$I = 4500\ mA\ (C = 0.1\ h^{-1})$	$V_{eoc} = 3800\ V$

Figure 22 shows the cell current and Figure 23 shows the cell voltage over time during the formation procedure. Initially the cell is charged with $I_{cell} = 900\ mA$. The voltage rises from $V_{cell} = 0\ V$ at the beginning of the formation, to $V_{eoc} = 4200\ mV$ at the end of the formation. During the first two hours of formation the cell is mechanically rolled every 30 minutes to press out gases that form during the cell formation process. The small voltage drops at $t = 0.5\ h$ and $t = 1\ h$ are caused by this mechanical stress. After the initial CC-charging a CV-charging is performed. Because of the low formation current, the CV-phase is very short. The majority of the formation reactions are completed after the first charging. Subsequently the cell is discharged. In the second cycle the charging current is increased to $I_{cell} = 4500\ mA$. After the following CV-phase the cell is discharged a second time. This discharging process is used to determine the capacity of the cell after formation:

$$Q = 2.004\ h \times 4500\ mA = 9.02\ Ah \qquad \textit{Eq. 4-2}$$

Finally, the cell is charged again until the termination criterion $V_{eoc} = 3800\,mV$ is reached. The last cycle leaves the cell at a SoC of 40%. This is necessary as lithium cells may neither be stored with a high, nor with a low state of charge.

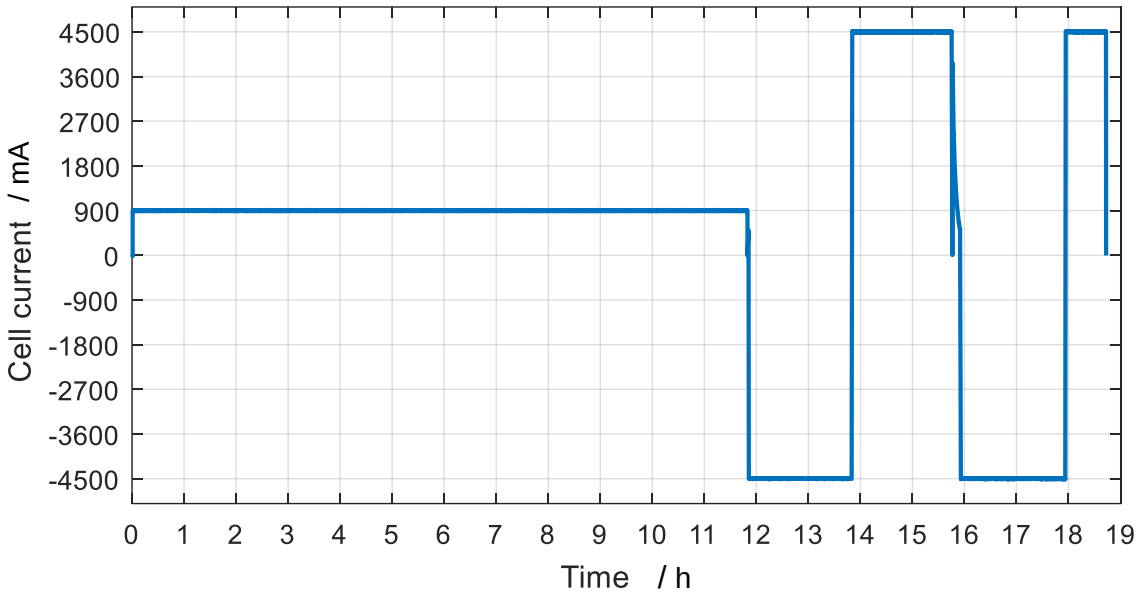

Figure 22: Cell current of the NMC pouch cell over time during formation and cycling

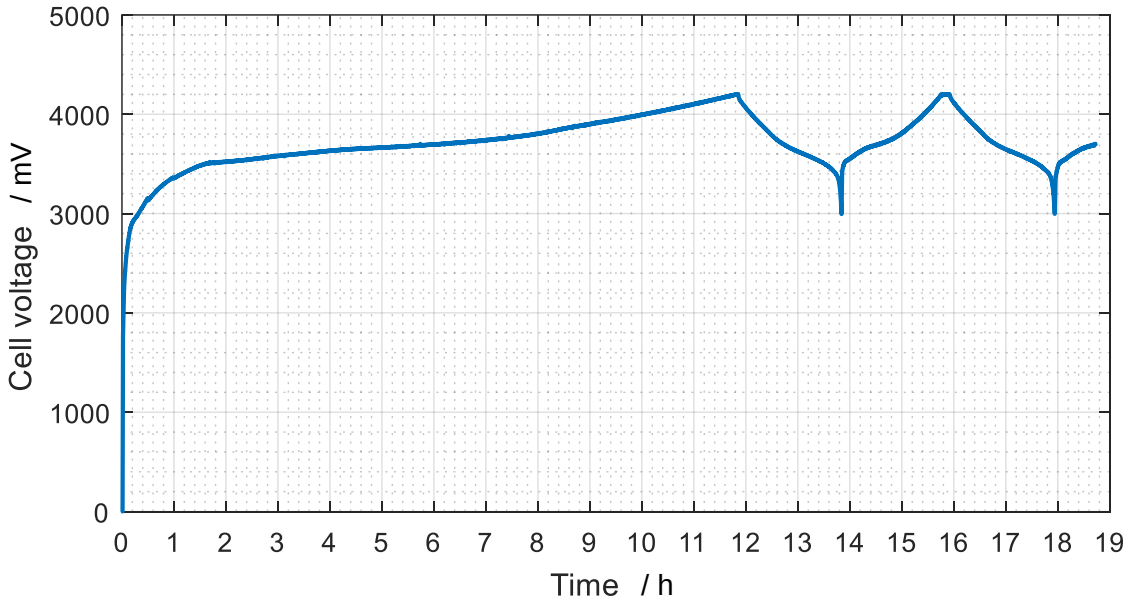

Figure 23: Cell voltage of the NMC pouch cell over time during formation and cycling

Figure 24 shows the voltage of the DC storage battery. While charging the lithium ion cell, the 12 V battery is discharged. This causes the battery voltage to decrease. The opposed effect can be

observed during discharging of the lithium cell: the battery voltage increases as this means charging the 12 V battery. Figure 25 shows the cell temperature over time. Owing to the fact, that the cell was not cycled under constant ambient climatic conditions, no direct conclusions can be drawn from the cell temperature. Nevertheless, it is monitored and logged to guarantee a safe operation of the cell. In combination with an ambient temperature measurement or formation in a climate cabinet, also conclusions regarding the formation process can be drawn as the cell temperature is an important influence factor for the SEI formation.

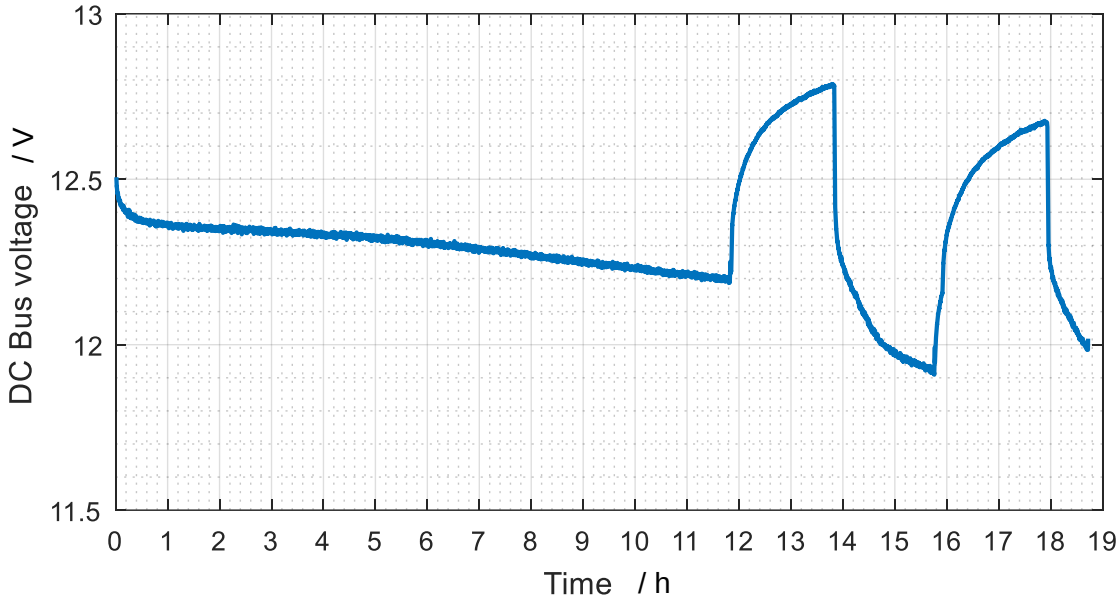

Figure 24: Voltage of the DC storage battery over time during formation and cycling

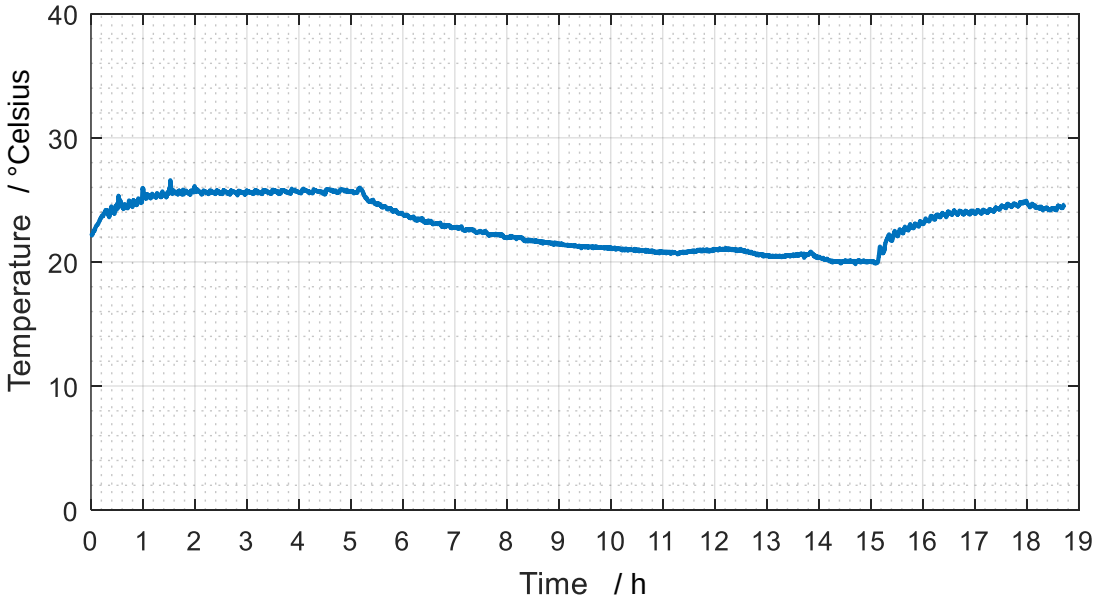

Figure 25: Cell temperature of the NMC pouch cell over time during formation and cycling

Thus, the aim of lithium ion cell formation with recuperation of the discharging energy is achieved. Depending on the electrical efficiency and cost structure it can be feasible to choose such a system over a non-recuperating one. These evaluations are done in the following chapters.

4.4 Electrical efficiency and energy recuperation

As outlined in chapter 3.4, the efficiency of the buck and boost converter, as well as the cycle efficiency for a full cycle was evaluated. Figure 26 shows the efficiency of the buck converter in the operating area of $I_{cell} = [0\ A, 10\ A]$ and $V_{cell} = [0\ V, 4.3\ V]$. In areas of very low cell current or very low cell voltage the efficiency is poor and falls below 50%. The reason is the internal energy consumption of the cell formation unit. The components that are accountable for the internal energy consumption are the microcontroller, gate-drivers, voltage regulators and a DC/DC converter for the high side gate driver. Apart from these peripheral zones the efficiency increases with cell voltage and decreases slightly with the cell current. The efficiency increase is caused by the increasing duty cycle with cell voltage as conducting losses of the diode are higher than conducting losses of the transistor. The efficiency decrease along with the cell current is caused by ohmic losses, that are quadratically dependent on the current. Additionally, the forward losses of the diode increase with the cell current because of the current dependency of the Schottky diode forward voltage. The maximum efficiency of $\eta = 0.79$ is reached for $I_{cell} = 3\ A$ and $V_{cell} = 4.3\ V$.

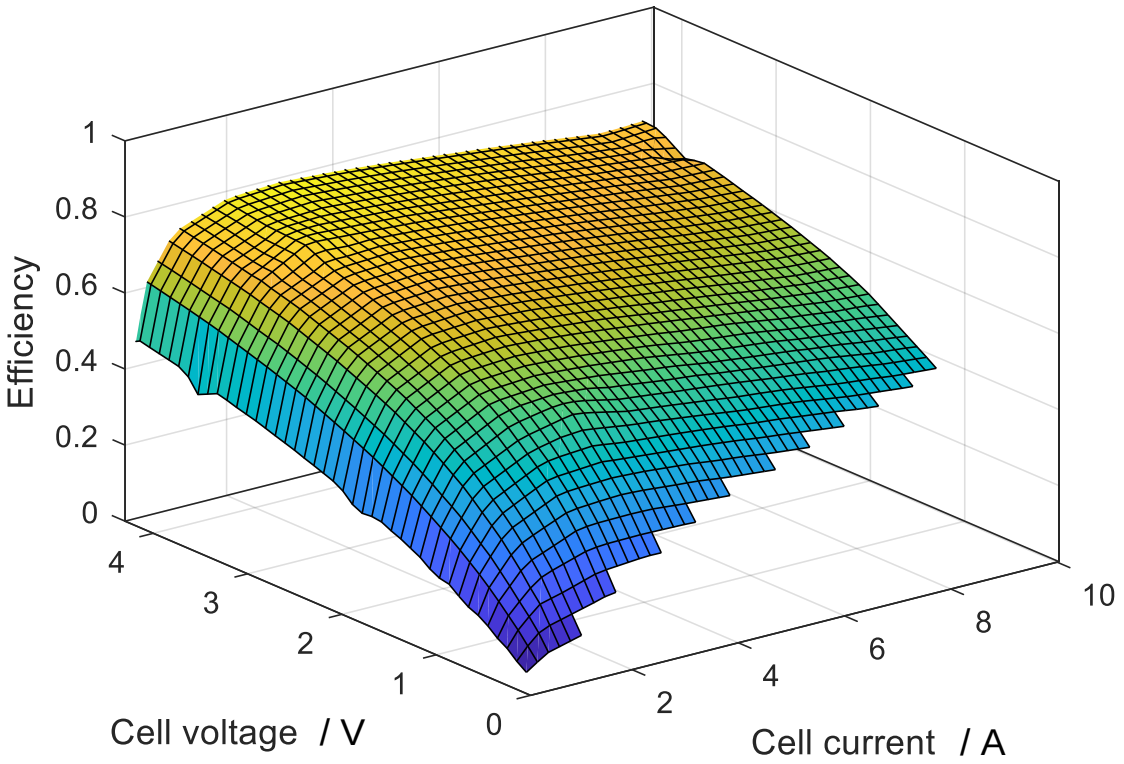

Figure 26: Efficiency of the cell formation unit in buck conversion (charging) mode

Apart from a very short time span during formation the cell voltage is higher than 2.0 V for LIP cells and 3.0 V for NMC cells (see chapter 4.3). Typical currents during formation range from $C = 0.1\ h^{-1}$ to $C = 0.5\ h^{-1}$. For a 10 Ah cell this means cell currents from $I_{cell} = [1\ A, 5\ A]$. Figure 27 shows the efficiency within this typical operating area. The total efficiency is between $\eta = 0.54$ and $\eta = 0.79$.

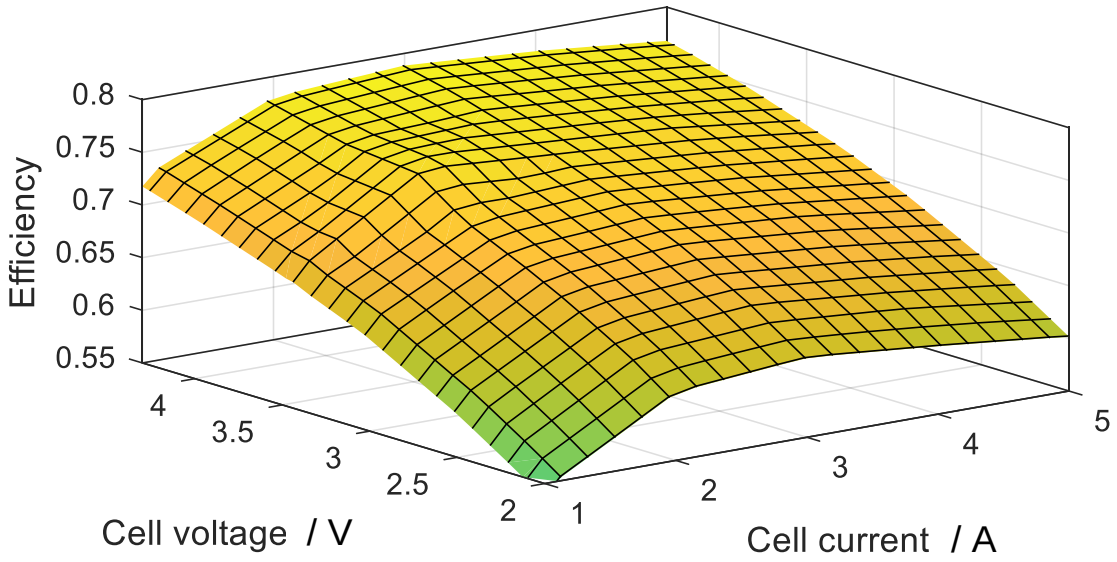

Figure 27: Efficiency of the cell formation unit in buck conversion (charging) mode in typical operation area

The boost converter is not used for the initial charging process during formation. For that reason, the input voltages of the boost converter stay within the specified minimum and maximum voltages of the cell. Figure 28 shows the efficiency map of the system in buck mode from $I_{cell} = [0\ A, 10\ A]$ and $V_{cell} = [2\ V, 4.3\ V]$. The efficiency map is similar to the buck-converter efficiency map, having a maximum at $I_{cell} = 3.5\ A$ with $\eta = 0.8$. Again, the efficiency for low currents is poor, as the converted power is low compared to the consumed power of the control circuits on the cell formation unit.

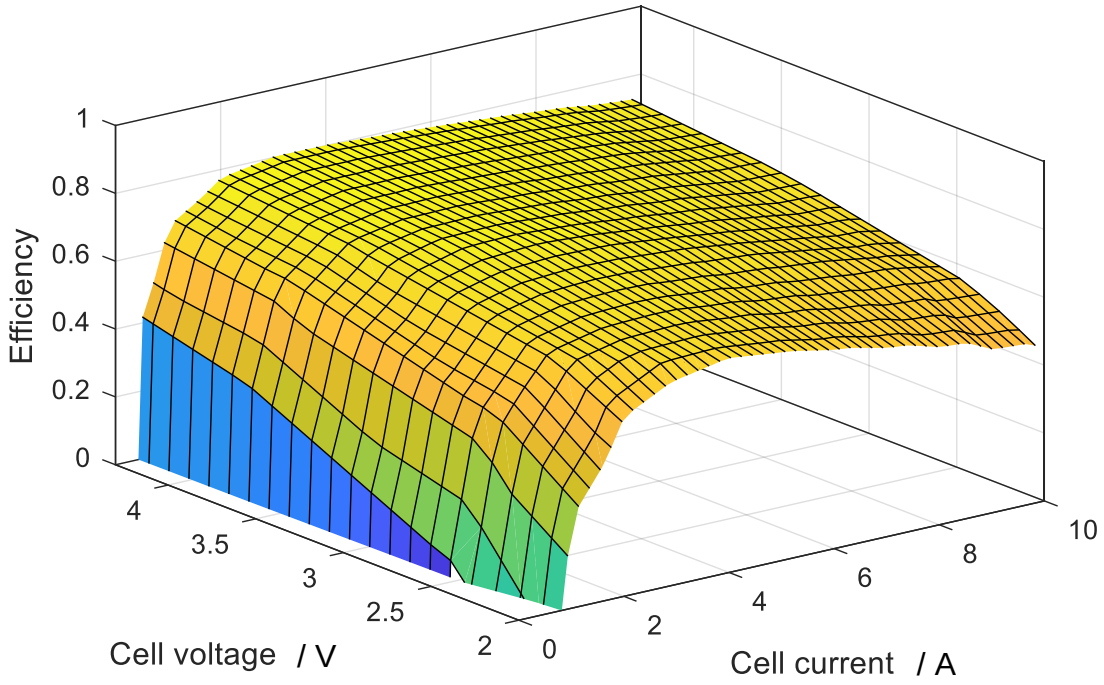

Figure 28: Efficiency of the cell formation unit in boost conversion (discharging) mode in typical operation area

With these efficiency maps, the cycle efficiency of the formation and charging cycle can be calculated according to chapter 3.4. For these calculations, the formation protocol of the 10Ah NMC lithium-ion cell in chapter 4.3 was used. To begin with, the formation efficiencies are

$$\eta_{charge} = \left|\frac{E_{cell}}{E_{source}}\right| = \frac{39.4\ Wh}{57.9\ Wh} \approx 0.68 \qquad \textit{Eq. 4-3}$$

and

$$\eta_{discharge} = \left|\frac{E_{sink}}{E_{cell}}\right| = \frac{25.8\ Wh}{33.5\ Wh} \approx 0.77 \qquad \textit{Eq. 4-4}$$

This means that 77% of the energy that is contained in the cell after formation are recuperated during discharging. The total cycle energy efficiency is

$$\eta_{cycle} = \left|\frac{E_{sink}}{E_{source}}\right| = \frac{25.8\ Wh}{57.9\ Wh} \approx 0.45 \qquad \textit{Eq. 4-5}$$

This means that 45% percent of the energy is recuperated from the formation cycle. Figure 30 shows the formation charging and the subsequent discharging with stepwise energy calculation.

For the efficiency calculation of a normal charging/discharging cycle the second cycle from chapter 4.3 is used. With Eq. 3-11 the efficiency of the charging procedure is

$$\eta_{charge} = \left|\frac{E_{cell}}{E_{source}}\right| = \frac{33.8\,Wh}{45.0\,Wh} \approx 0.75 \qquad \textit{Eq. 4-6}$$

and the discharging efficiency is

$$\eta_{discharge} = \left|\frac{E_{sink}}{E_{cell}}\right| = \frac{25.8\,Wh}{33.5\,Wh} \approx 0.77 \qquad \textit{Eq. 4-7}$$

The cycle efficiency is

$$\eta_{cycle} = \left|\frac{E_{sink}}{E_{source}}\right| = \frac{25.8\,Wh}{45.0\,Wh} \approx 0.57 \qquad \textit{Eq. 4-8}$$

This means that 57% of the energy, that is needed for charging, can be recuperated during discharging. For comparison, the BaSyTec XCTS, which is a commercially available cell formation system with energy recuperation using a DC/AC inverter reaches a charging efficiency up to 85% and a discharging efficiency up to 65% [9]. This leads to a maximum cycle efficiency of 55%. Figure 31 shows the formation charging and the subsequent discharging with stepwise energy calculation. The cycle efficiency of the charging cycle is higher than the cycle efficiency of the formation because a certain amount of energy is needed for the SEI formation reactions, as explained in chapter 2.1.4. Furthermore, the efficiency is higher because of the higher charging current compared to the formation: Figure 29 shows the buck converter efficiency for a cell current of $I = 4500\,mA$ versus a cell current of $I = 900\,mA$. Contrary to the charging efficiency, the discharging efficiency shows now difference.

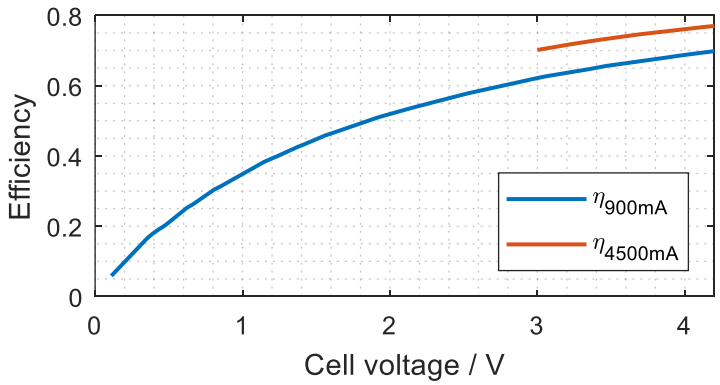

Figure 29: Efficiency of the boost converter for different charging currents

Based on these energy calculations the dimensioning of the 12 V storage system can be performed. The amount of energy needed for one cycle is determined by the difference between the energy consumption for charging and recuperated energy from discharging.

For a formation cycle of the 10 Ah NMC cell this accounts for

$$E_{cycling} = 57.9\,Wh - 25.8\,Wh = 32.1\,Wh \qquad \textit{Eq. 4-9}$$

For a charging/discharging cycle of the 10 Ah NMC cell this accounts for

$$E_{cycling} = 45.0\,Wh - 25.8\,Wh = 19.2\,Wh \qquad \textit{Eq. 4-10}$$

This means that the capacity of the 12 V storage must be dimensioned with at least 57.9 Wh (≈ 4.8 Ah @ 12 V) for the initial formation process and additionally 19.2 Wh (= 1.6 Ah @ 12V) for each additional cycle. This leaves a rest capacity of 32.1 Wh (≈ 4.7 Ah @ 12 V). If cells with higher capacities shall be cycled, the capacity of the 12 V storage must be scaled up accordingly. Additionally, a safety factor compensating capacity loss due to aging of the lead acid battery is recommended. As a consequence of dimensioning in accordance with these criteria the 12 V storage has to be recharged after every formation and cycling process. If a lower charging frequency of the storage battery is demanded, is must be increased accordingly. Increasing the storage capacity is sensible for another reason: The lifetime of a lead-acid battery depends on the depth-of-discharge. Using a battery with a higher capacity leads to lower DoD states and therefore increasing cycle life. Under these boundary conditions a capacity of 33 Ah per channel is reasonable.

Still, the efficiency of buck and boost conversion should be improved. This can be achieved by operating the cell formation unit with synchronous rectification as outlined in chapter 2.2.3. The hardware requirements for synchronous rectification are provided. Moreover, the reduction of the switching frequency will reduce the switching losses. Simultaneously the inductance of the choke must be increased if the current ripple shall not be changed. This includes adaption of the control system, as this modification will change the control loop characteristics. With increasing efficiency, not only the storage can be dimensioned smaller, but also the economic conclusions, which are discussed in the following chapter, might change.

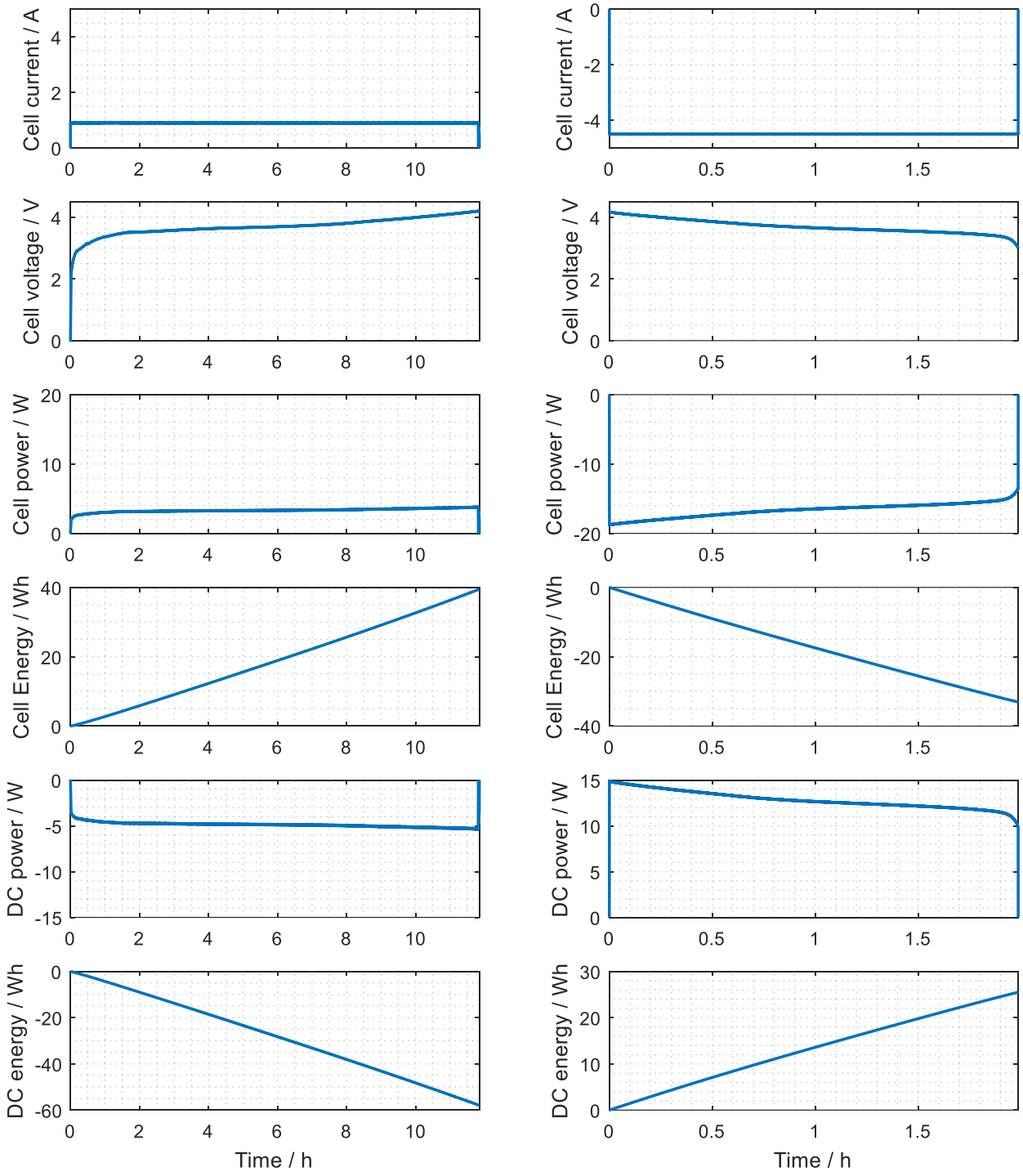

Figure 30: Cycle efficiency evaluation of the formation

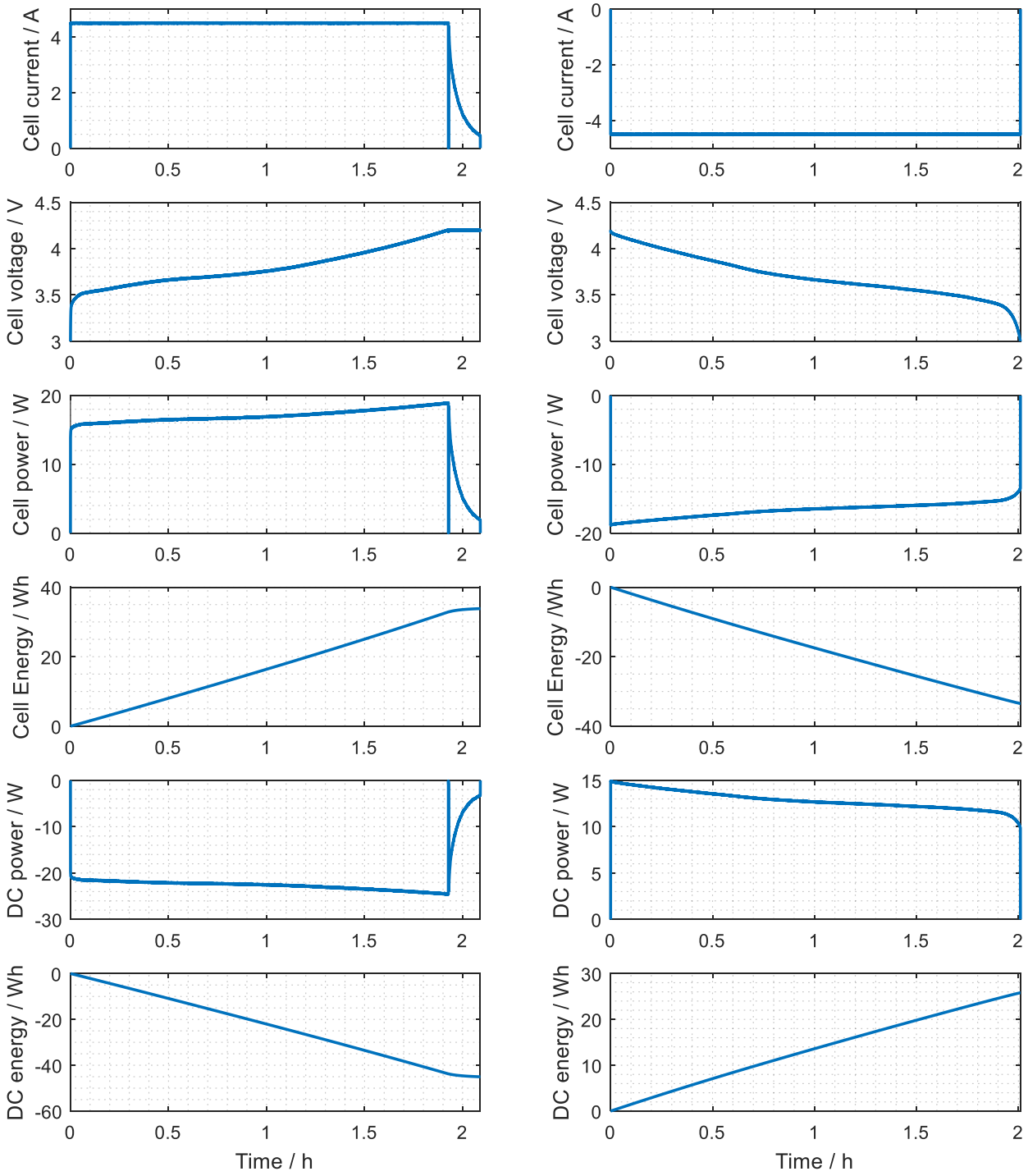

Figure 31: Cycle efficiency evaluation of the second cycle

4.5 Economic evaluation

For the LCOS analysis the benchmark cycle from Figure 2 in chapter 2.1.4 was used. The required energy for formation and cycling is calculated using the results from chapter 4.4. Every full benchmark process draws an amount of energy of

$$E_{source} = 57.9\ Wh + 2 \times 45\ Wh + 25Wh = 172.9\ Wh. \quad \textit{Eq. 4-11}$$

With 2000 cycles per year at a storage voltage of 12 V this is a cumulated discharge of

$$Q = \frac{167.9\ Wh}{12\ V} \times 2000 = 28{,}817\ Ah \quad \textit{Eq. 4-12}$$

With this value the number of cycles for each battery capacity and the LCOS are calculated. Table 7 shows the number of cycles per year, the number of cycles over the lifetime of the system and LCOS for different storage batteries. As it can be seen from the results, the shared lead-acid battery with a capacity of 260 Ah has the lowest LCOS of all batteries. The advantage over eight 35 Ah batteries is its lower price per Ah. The LIP technology cannot play its strength in cycle life, simply because the end-of-life criteria is not reached for any of the batteries.

Table 7: Number of cycles and LCOS for different storage batteries

Type	*Cycles per year*	*Cycles in 10 years*	*LCOS in* € / kWh
Siga S35-12 AGM, Pb	121.1	1211	0.39
Siga S260-12 AGM, Pb	130.4	1304	0.28
Super B SB12V100E, LIP	303.3	3033	0.97
Victron Energy BMS, LIP	189.6	1896	0.95

It must be noted that these values cannot be compared with the electricity price from the grid as they are not LCOE but LCOS.

For the assessment of a specific investment case the payback period according to Eq. 2-35 was calculated with the cost structure from Table 4. With the results from chapter 4.4 the energy reduction of the benchmark case can be calculated. The consumption is reduced from 172.9 Wh to

95.5 Wh per benchmark cycle, which equals a reduction of 44.8%. The application of 2000 benchmark cycles per year this leads to an annual consumption of 385.8 kWh compared to 191 kWh. The payback period of the 12 V VRLA-AGM battery with a capacity of 260 Ah is

$$payback\ period = \frac{469.5\ €}{(385.8\ kWh - 191\ kWh) \times 0.17\ \frac{€}{kWh} \times y^{-1}} = 14.18\ y \qquad \textit{Eq. 4-13}$$

The payback period exceeds the lifetime of the system and the maximum cycle life of the storage battery. The realization of the system is not economically viable under the given circumstances. Nevertheless, this can change if the costs of a cooling system are considered. Additionally, a further optimization of the storage battery dimensioning can lead to a shorter payback period. Another significant potential for improvement is the efficiency of the cell formation system. Moreover, a more sophisticated cell management is conceivable. If the cycles are coordinated so that charging and discharging of cells is done simultaneously, the storage battery can be dimensioned smaller, as the net energy delivered by the storage is reduced.

For this economic assessment a large number of input parameters were considered. Many of them have great influence on the result, such as the number of formed and cycled cells, the cell formation efficiency, and the storage battery DoD which results from the capacity dimensioning of the battery storage. As a consequence, it is essential to conduct a sensitivity analysis of the input data and specify constraints concerning the desired operation strategy. A Monte Carlo analysis could be a method to assess these uncertainties. Furthermore, dynamic capital budgeting methods should be used to determine the viability in specific use cases. Apart from the economic assessment other interesting questions are worth pursuing. A lifecycle analysis (LCA) to compare the environmental impact of the battery system with the fuel mix disclosure of power grid electricity or the calculation of the energy payback times of the battery system are only two examples.

5 Conclusion and Outlook

The aim of this thesis was to develop a cell formation system that provides energy recuperation from the discharging process of lithium ion cells during formation and cycling. A cell formation unit with a 12 V intermediate storage battery was built up, commissioned and characterized. In detail, an early hardware prototype was revised, commissioned and programmed. A PID controller was developed and implemented for current and voltage control. The heuristic Ziegler-Nichols method was used for controller tuning. To guarantee the safe operation of the system a battery management system with eight channels was built. The fully interrupt driven firmware of the cell formation unit and the firmware of battery management system was implemented in C using a CAN bus for communication and logging. The high-level system control was developed in MATLAB.

The cell formation system was characterized in charging mode and in discharging mode regarding the implemented control system and its efficiency in buck and boost mode. A LIP cell was cycled and a NMC cell was formed and cycled. Additionally, the cycle efficiency and recuperation potential of a formation cycle and a charging cycle was evaluated. The energy recuperation potential amounts to 45% for formations and 57% for cycling. An economic assessment was realized with the LCOS method to determine the cost of different storage options and the payback period of the recuperation system was calculated. Under the given circumstances the cell formation system with energy recuperation is not economically viable. To back up this verdict, a sensitivity analysis is proposed. The results might change with the integration of cooling cost into the capital budgeting method. Furthermore, an increase of the cell formation unit’s efficiency and a storage optimization will probably lead to different results.

To advance the performance of the system in further works, the improvement of the efficiency should be the priority. This can be achieved by decreasing the switching frequency or implementing a synchronous converter control. Furthermore, the system should be extended to more than one channel. The software requirements for this extension are complied with. The battery management system should be extended with an overcurrent protection to integrate all protection functions into the BMS. In this step it makes sense to migrate the battery management system from its prototype status to a standalone system with microcontroller and discrete analog-to-digital converters which delivers higher measurement resolution. Furthermore, an economic optimization of 12V the intermediate storage is necessary, depending on the number of channels.

References

[1] A. Palzer and H.-M. Henning, *What will the energy transformation cost? Pathways for transforming the German energy system by 2050*, 2015.

[2] A. Thielmann, A. Sauer, and M. Wietschel, *Gesamt-Roadmap Lithium-Ionen-Batterien 2030*. Karlsruhe, 2015.

[3] B. Dunn, H. Kamath, and J.-M. Tarascon, "Electrical Energy Storage for the Grid: A Battery of Choices," *Science*, vol. 334, no. 6058, p. 928, 2011.

[4] P. Kurzweil and O. K. Dietlmeier, *Elektrochemische Speicher: Superkondensatoren, Batterien, Elektrolyse-Wasserstoff, rechtliche Grundlagen*. Wiesbaden: Springer Vieweg, 2015.

[5] H. Budde-Meiwes *et al.*, "A review of current automotive battery technology and future prospects," *Proceedings of the Institution of Mechanical Engineers, Part D: Journal of Automobile Engineering*, vol. 227, no. 5, pp. 761–776, 2012.

[6] A. Väyrynen and J. Salminen, "Lithium ion battery production," *The Journal of Chemical Thermodynamics*, vol. 46, pp. 80–85, 2012.

[7] N. Nitta, F. Wu, J. T. Lee, and G. Yushin, "Li-ion battery materials: Present and future," *Materials Today*, vol. 18, no. 5, pp. 252–264, 2015.

[8] D. L. Wood, J. Li, and C. Daniel, "Prospects for reducing the processing cost of lithium ion batteries," *Journal of Power Sources*, vol. 275, pp. 234–242, 2015.

[9] BaSyTec GmbH, *BaSyTec XCTS: Cell Test and Formation System.* [Online] Available: http://www.basytec.de/prospekte/Basytec%20XCTS%202016_04.pdf. Accessed on: Nov. 01 2017.

[10] Chroma ATE, *Battery Cell Charge & Discharge: Test System Model 17011*. [Online] Available: http://www.chromaus.com/datasheet/17011-E-201606.pdf.

[11] R. Korthauer, Ed., *Handbuch Lithium-Ionen-Batterien*. Berlin, Heidelberg, s.l.: Springer Berlin Heidelberg, 2013.

[12] N. Bensalah and H. Dawood, "Review on Synthesis, Characterizations, and Electrochemical Properties of Cathode Materials for Lithium Ion Batteries," *J Material Sci Eng*, vol. 5, no. 4, 2016.

[13] R. Younesi, G. M. Veith, P. Johansson, K. Edström, and T. Vegge, "Lithium salts for advanced lithium batteries: Li–metal, Li–O 2 and Li–S," *Energy Environ. Sci.*, vol. 8, no. 7, pp. 1905–1922, 2015.

[14] S. S. Zhang, “A review on the separators of liquid electrolyte Li-ion batteries,” *Journal of Power Sources*, vol. 164, no. 1, pp. 351–364, 2007.

[15] P. Verma, P. Maire, and P. Novák, “A review of the features and analyses of the solid electrolyte interphase in Li-ion batteries,” *Electrochimica Acta*, vol. 55, no. 22, pp. 6332–6341, 2010.

[16] P. B. Balbuena and Y. Wang, Eds., *Lithium-ion batteries: Solid-electrolyte interphase*. London: Imperial College Press, 2007.

[17] S. J. An *et al.*, “The state of understanding of the lithium-ion-battery graphite solid electrolyte interphase (SEI) and its relationship to formation cycling,” *Carbon*, vol. 105, pp. 52–76, 2016.

[18] S. Zhang, K. Xu, and R. Jow, “EIS study on the formation of solid electrolyte,” *Electrochimica Acta*, vol. 51, 2006.

[19] M. Wolter, G. Fauser, C. Bretthauer, and M. A. Roscher, “End-of-line testing and formation process in Li-ion battery assembly lines,” in *International Multi-Conference on Systems, Sygnals & Devices*, Chemnitz, Germany, 2012, pp. 1–3.

[20] Z. Chu *et al.*, “Non-destructive fast charging algorithm of lithium-ion batteries based on the control-oriented electrochemical model,” *Applied Energy*, vol. 204, pp. 1240–1250, 2017.

[21] T. Ohsaki *et al.*, “Overcharge reaction of lithium-ion batteries,” *Journal of Power Sources*, vol. 146, no. 1-2, pp. 97–100, 2005.

[22] F. Zach, *Leistungselektronik: Ein Handbuch*, 5th ed. Wiesbaden: Springer Vieweg, 2015.

[23] B. L. Dokić and B. Blanuša, *Power Electronics: Converters and Regulators*, 3rd ed. Cham, s.l.: Springer International Publishing, 2015.

[24] U. Schlienz, *Schaltnetzteile und ihre Peripherie: Dimensionierung, Einsatz, EMV*, 3rd ed. Wiesbaden: Friedr. Vieweg & Sohn Verlag | GWV Fachverlage GmbH Wiesbaden, 2007.

[25] J. Lunze, *Regelungstechnik 1: Systemtheoretische Grundlagen, Analyse und Entwurf einschleifiger Regelungen*, 11th ed. Berlin, Heidelberg: Springer Berlin Heidelberg, 2016.

[26] S. Matlok, B. Eckardt, B. Seliger, and M. Maerz, “Digital Control of Hard Switched Converters by Phase Modulated Pulse Width Modulation PMPWM,” in *PCIM Europe 2017; International Exhibition and Conference for Power Electronics, Intelligent Motion, Renewable Energy and Energy Management*, 2017, pp. 1–8.

[27] A. Visioli, “Modified anti-windup scheme for PID controllers,” *IEE Proceedings - Control Theory and Applications*, vol. 150, no. 1, pp. 49–54, 2003.

[28] J. E. Larsson, “A simple antiwindup method,” *International Journal of Control*, vol. 60, no. 5, pp. 1025–1033, 1994.

[29] C. Bohn and D. P. Atherton, “An analysis package comparing PID anti-windup strategies,” *IEEE Control Syst. Mag.*, vol. 15, no. 2, pp. 34–40, 1995.

[30] H. Mann, H. Schiffelgen, and R. Froriep, *Einführung in die Regelungstechnik: Analoge und digitale Regelung, Fuzzy-Regler, Regler-Realisierung, Software*, 11th ed. München: Hanser, 2009.

[31] S. Brich, Ed., *Gabler Wirtschaftslexikon*, 18th ed. Wiesbaden: Springer Gabler, 2014.

[32] J. Wang *et al.*, “Cycle-life model for graphite-LiFePO4 cells,” *Journal of Power Sources*, vol. 196, no. 8, pp. 3942–3948, 2011.

[33] P. Ruetschi, “Aging mechanisms and service life of lead–acid batteries,” *Journal of Power Sources*, vol. 127, no. 1-2, pp. 33–44, 2004.

[34] M. Zapf, *Stromspeicher und Power-to-Gas im deutschen Energiesystem: Rahmenbedingungen, Bedarf und Einsatzmöglichkeiten*. Wiesbaden: Springer Vieweg, 2017.

[35] V. Jülch, “Comparison of electricity storage options using levelized cost of storage (LCOS) method,” *Applied Energy*, vol. 183, pp. 1594–1606, 2016.

[36] P. Konstantin, *Praxisbuch Energiewirtschaft: Energieumwandlung, -transport und -beschaffung im liberalisierten Markt*, 3rd ed. Berlin, Heidelberg, s.l.: Springer Berlin Heidelberg, 2013.

[37] C. Thibierge and A. Beresford, *A Practical Guide to Corporate Finance: Breaking the Financial Ice*. Basingstoke: Palgrave Macmillan, 2015.

[38] U. Götze, *Investitionsrechnung: Modelle und Analysen zur Beurteilung von Investitionsvorhaben*, 7th ed. Berlin: Springer Gabler, 2014.

[39] STMICROELECTRONICS, “AN4073: How to improve ADC accuracy when using STM32F2xx and STM32F4xx microcontrollers,”

[40] R. J. Brodd, Ed., *Batteries for Sustainability: Selected Entries from the Encyclopedia of Sustainability Science and Technology*. New York, NY: Springer, 2013.

[41] R. R. Asche, *Embedded Controller: Grundlagen und praktische Umsetzung für industrielle Anwendungen*. Wiesbaden: Springer Fachmedien Wiesbaden, 2016.

[42] SUPER B B.V., *Datasheet SB12V160E-ZC*. [Online] Available: http://www.super-b.com/content/files/Files/Products/SB12V160E-ZC_book.pdf. Accessed on: Nov. 04 2017.

[43] SIGA Batterien, *Datasheet SIGA S260-12.* [Online] Available: http://www.siga-batterien.de/Datenblatt/S260-12.pdf. Accessed on: Nov. 04 2017.

[44] SIGA Batterien, *Datasheet SIGA S35-12.* [Online] Available: http://www.siga-batterien.de/Datenblatt/S35-12.pdf. Accessed on: Nov. 04 2017.

[45] Victron Energy B.V., *Datasheet Victron Energy LFP-BMS 12.8/160.* [Online] Available: https://www.victronenergy.com/upload/documents/Datasheet-12,8-Volt-lithium-iron-phosphate-batteries-EN.pdf. Accessed on: Nov. 04 2017.

[46] Bundesverband der Energie- und Wasserwirtschaft e.V., *BDEW-Strompreisanalyse Mai 2017: Haushalt und Industrie.* [Online] Available: https://www.bdew.de/internet.nsf/res/ACB6766AE4CA66E0C1258132004BC873/$file/170531_BDEW_Strompreisanalyse_Mai2017.pdf.

Table of Figures

Figure 1: Illustration of a lithium ion cell: (a) aluminum current collector (positive electrode), (b) oxide active material, (c) porous separator, (d) solid-electrolyte interface, (e) graphite active material, (f) copper current collector (negative electrode) [15] 4
Figure 2: Cell formation of a 10 Ah lithium-ion pouch cell 8
Figure 3: Schematics of the boost converter 10
Figure 4: State of the switch S and choke current over time 11
Figure 5: Normalized current ripple as a function of the duty cycle D 12
Figure 6: Schematics of the boost converter 13
Figure 7: Synchronous converter schematics 15
Figure 8: Bidirectional power flow in quadrant I + II (shaded area) 15
Figure 9: Basic structure of a closed loop control system [25] 16
Figure 10: System architecture overview 22
Figure 11: Battery management system schematic of one channel 25
Figure 12: Laboratory setup for the formation of a 10 Ah lithium ion cell (NMC) 26
Figure 13: Schematic chronological order of measurement, control algorithm, and duty cycle set 29
Figure 14: Cell formation unit firmware structure 29
Figure 15: Step response of the closed loop current control in buck mode (charging) 39
Figure 16: Step response of the closed loop current control in boost mode (discharging) 40
Figure 17:Step response of the closed loop voltage control in buck mode (charging) 41
Figure 18: Cell voltage of lithium-iron-phosphate cell over time 42
Figure 19: Cell current of the lithium iron phosphate cell over time 43
Figure 20:Voltage of the 12V DC-bus lead acid battery over time 44
Figure 21: Temperature of lithium-iron-phosphate cell over time 44
Figure 22: Cell current of the NMC pouch cell over time during formation and cycling 46
Figure 23: Cell voltage of the NMC pouch cell over time during formation and cycling 46
Figure 24: Voltage of the DC storage battery over time during formation and cycling 47
Figure 25: Cell temperature of the NMC pouch cell over time during formation and cycling 47
Figure 26: Efficiency of the cell formation unit in buck conversion (charging) mode 49
Figure 27: Efficiency of the cell formation unit in buck conversion (charging) mode in typical operation area 50

Figure 28: Efficiency of the cell formation unit in boost conversion (discharging) mode in typical operation area 51
Figure 29: Efficiency of the boost converter for different charging currents 52
Figure 30: Cycle efficiency evaluation of the formation 54
Figure 31: Cycle efficiency evaluation of the second cycle 55

List of Tables

Table 1: Charging energy, discharging energy and relative energy loss for cycle 1-4 8
Table 2: Parametrization according to Ziegler and Nichols [25] 18
Table 3: Parameter overview of selected battery types for intermediate storage [42–45] 37
Table 4: Overview of the relevant component costs for the payback period calculation 38
Table 5: LIP cell cycling protocol 41
Table 6: Protocol of the formation and cycling of a 10 Ah NMC cell 45
Table 7: Number of cycles and LCOS for different storage batteries 56

Listings

Listing 1: Listing of the reduced BMS code in C 30
Listing 2: Pseudocode of the MATLAB control algorithm 32